STM Studies of Nano-Structures.

A thesis submitted to the University of Manchester for the degree of PhD

in the Faculty of Engineering and Physical Sciences

2006

Matthew Johns-Chapman

School of Physics and Astronomy

Table of Contents

Table of Figures

Table of Tables

List of Abbreviations

2-DEG	Two Dimensional Electron Gas
AC	Alternating Current
ADC	Analogue to Digital Converter
AFM	Atomic Force Microscope/Microscopy
Ag	Silver
Al2O3	Sapphire
AlAs	Aluminium Arsenide
AlGaAs	Aluminium Gallium Arsenide
Au	Gold
CAFM	Conducting Atomic Force Microscope/Microscopy
CFM	Capacitance Force Microscope/Microscopy
DC	Direct Current (also use to refer to a steady or slowly varying non-AC signal)
DOS	Density Of States
DSP	Digital Signal Processor
FFT	Fast Fourier Transform
GaAs	Gallium Arsenide
GaN	Gallium Nitride
H	Hydrogen
He-Ne	Helium Neon (a gas mixture used as the medium in a common gas laser)
HF	HydroFluoric Acid
HV	High Vacuum
HVPE	Hydride Vapour Phase Epitaxy
IC-AFM	Intermittent Contact mode Atomic Force Microscope/Microscopy
InGaN	Indium Gallium Nitride
KOH	Potassium Hydroxide
KPFM	Kelvin Probe Force Microscope/Microscopy
LD	Laser Diode
LDOS	Local Density Of States
LED	Light Emitting Diode
LEEBI	Low Energy Electron Beam Irradiation
LIA	Lock In Amplifier

LTSTM	Low Temperature Scanning Tunnelling Microscope/Microscopy
LV	Low Vacuum
MBE	Molecular Beam Epitaxy
MFM	Magnetic Force Microscope/Microscopy
Mg	Magnesium
MOCVD	Metal Organic Chemical Vapour Deposition
MOVPE	Metal Organic Vapour Phase Epitaxy
MQW	Multiple Quantum Well
MV	Medium Vacuum
NaOH	Sodium Hydroxide
NC-AFM	Non Contact mode Atomic Force Microscope/Microscopy
NH3	Ammonia
Pt-Ir	Platinum-Iridium
QW	Quantum Well
SEM	Scanning Electron Microscope/Microscopy
Si	Silicon
SNOM	Scanning Near Field Microscope/Microscopy
SPM	Scanning Probe Microscope/Microscopy
STEM	Scanning Transmission Electron Microscope
STM	Scanning Tunnelling Microscope/Microscopy
TEM	Transmission Electron Microscope
TFM	Torsional Force Microscope/Microscopy
Trike	Trichloroethylene
TSP	Titanium/Tantalum Sublimation Pump
UHV	Ultra High Vacuum
W	Tungsten
WKB	Wentzel Kramers Brillouin (also known as WKBJ, the J is for Jeffreys)
X-STM	Cross Sectional Scanning Tunnelling Microscope/Microscopy
Zn	Zinc

The University of Manchester

ABSTRACT OF THESIS submitted by Matthew Johns-Chapman.

for the Degree of PhD and entitled STM Studies of Nano-Structures.

Month and Year of Submission April 2006.

This thesis embodies research performed on a number of novel materials with nanometre scale electronic features using the powerful scanning probe microscopy techniques; with a strong focus on STM (Scanning Tunnelling Microscopy).

The materials studied are a novel gallium arsenide based photosensitive nano-structure with uses in Terra-Hertz signal modulation and a set of gallium nitride based multiple quantum well materials used to understand the properties of modern blue light emitting diodes and laser diodes.

The techniques used and developed for this work are based upon scanning tunnelling microscopy and atomic force microscopy. A novel photoenhanced scanning tunnelling microscopy technique was also used.

The objective of this work is that of material characterisation and understanding, and the development and functionality of modern scanning probe microscopy techniques.

A set of materials have been characterised and some interesting electronic properties studied along with the development of photoenhanced STM techniques and material preparation methods.

Declaration.

No portion of the work referred to in the thesis has been submitted in support of an application for another degree or qualification of this or any other university or other institute of learning.

Copyright Statement.

Acknowledgements

I would like to thank all of the people who have helped me along the journey so far, including my supervisor Professor Bruce Hamilton whose advice and optimism have been well received and Eric Whittaker whose skills and dedication are inspired an appreciated. I would also like to thank Dr Philip Dawson for supplying sample materials and providing valuable consultation, and Dr Darren Graham for his level headed advice and encouragement. Thanks also to Stefan Birner for his assistance with the Nextnano3 software.

I would like to thank my family for their encouragement, including my mother who has always believed in me and my grandad who has always supported and encouraged me.

To my friends who have remained loyal throughout the years, thanks, and in particular to Sarah, for her patience and encouragement.

Chapter 1: Introduction

In 1947 researchers at Bell-Labs created the first transistor[1-3], this invention has been arguably the cornerstone of the modern information era, it has led to the creation of the wealth of semiconductor devices that followed, which includes the microprocessor, the solid state amplifier and numerous optoelectronic devices.

This modern technology has made the world a smaller place, metaphorically speaking. With it we are able to communicate and share information faster than ever before. It is the technology that has driven the communication and information revolution that in itself is also becoming smaller. The very devices which process and shift information are becoming smaller, more complex and more powerful. The increase in necessity and diversity has led to new, more demanding requirements from these devices, and so, drives research into new materials and technology to solve current problems more efficiently and take on the challenges of the future.

Novel materials and structures are investigated with device potential in mind and where such research will further current knowledge of such materials and more fundamental physics. Nanotechnology is one of the frontiers of semiconductor physics: it has gained a lot of press, promising to revolutionise the world we live in. While applications in medical science such as nano-scale robots to repair the human body may be a long way into the future, current microchip fabrication processes are already operating at 65nm[4] and current epitaxial growth techniques are capable of depositing single layers of atoms.

In this research, nano-scale devices will be examined and investigated using tools such as the STM (Scanning Tunnelling Microscope) to delve into the nano-scale world and investigate the properties of these structures and devices. The STM is the first of a number of scanning probe microscopies to emerge in the past 25 years, it has the unparalleled ability to image real space electronic and topographical information of a conducting or semiconducting material's surface on a sub-nanometre scale. The second major development in scanning probe techniques was the invention of the AFM

(Atomic Force Microscope) which provided purely topographical information for material surfaces including electrical insulators and the surfaces of liquid and biological material. Since these inventions a plethora of related techniques have emerged.

This thesis is composed of a set of chapters concerning the relevant methods used and materials investigated. The chapter on experimental techniques describes the systems and materials used to perform experiments, the chapter covers the technologies behind vacuum systems, the STM and AFM and related techniques, and the preparation of materials and probes for investigation. The mixed type I – type II GaAs AlAs material chapter concerns experiments performed on a novel multiple quantum well structure. STM was used to investigate the electronic and photoelectric properties of this material system and provide a greater understanding of its properties. The InGaN GaN multiple quantum well chapter reports on efforts made to understand the nature of spatial localisation of excitons within the quantum wells. The localisation is widely believed to allow operation of light emitting diodes (LED) and laser diodes (LD) based upon InGaN quantum well systems with high defect densities. The results obtained through this work will be summarised in the final chapter.

1.1 References

1 J. Bardeen and W.H. Brattain *Phys. Rev.* **1948**, *74(2)*, 230.

2 W.H. Brattain and J. Bardeen *Phys. Rev.* **1948**, *74(2)*, 231.

3 W. Shockley and G. L. Pearson *Phys. Rev.* **1948**, *74(2)*, 232.

4 Intel, press release, **Aug. 30, 2004**.

Chapter 2: Experimental Techniques

2.1 Introduction

A scientist requires a set of tools and procedures which are designed and implemented in such a way as to ensure that the results of the research are accurate and unambiguous. In this chapter the equipment and procedures used in this research will be described and discussed.

2.2 Vacuum Techniques

In certain situations and in order to perform specific tasks a vacuum is desirable. Many different disciplines use vacuums for their specific purposes but often the function of a vacuum is to provide a clean environment, free from contamination, in which to conduct a controlled experiment. A perfect vacuum is not achievable since even a stray atom invalidates this and the conditions necessary to achieve perfection are unachievable. The temperature would need to be absolute zero and the space void of photons and any other low interaction particles, such as neutrinos. The nearest vacuum to perfection known is intergalactic space, where there are only a few atoms per cubic meter. It is possible, however, to achieve a partial vacuum, which is adequate for the purposes of this research and beyond. In 1656 Otto von Guerikce performed an early vacuum experiment involving the demonstration of atmospheric pressure to seal two evacuated bronze hemispheres together[1]. The Magdeberg experiment and the pumps used to evacuate the hemispheres constituted a cornerstone of vacuum technology.

Following is a table representing the different levels of partial vacuum.

Vacuum	*Pressure (Torr)*
Low Vacuum	760 – 25
Medium Vacuum	25 – 10^{-3}
High Vacuum	10^{-3} – 10^{-6}
Ultra High Vacuum	10^{-9} and lower

Table 2.2-1: Pressures for different vacua.

2.2.1 Vacuum Pumps

There are two main types of pump used in this research to evacuate the chambers of the experimental apparatus. The first is the displacement pump such as the rotary-vane and the turbomolecular pump, the other is the trap type pump such as the ion pump and the sublimation pump. The rotary-vane pump (rotary pump) is the main pump used to expel large volumes of gas from the chambers. It operates from atmospheric pressure down to 10^{-3} torr by a mechanical means to move air from the inlet to the exhaust.

The second pump in the systems used is the turbomolecular pump (turbo pump), this is another mechanical displacement pump, designed around the operation of a turbine, which, is driven by a high speed motor in a low friction environment to convert the mechanical energy of the motor into directed kinetic energy of the gas. The turbo

pump's blades spin at typically tens of thousands of revolutions per minute at these speeds only very high energy molecules will be able to escape the pump. At typical operating temperatures this is a very low proportion of gas molecules. The turbo pump is capable of maintaining UHV (Ultra High Vacuum) conditions on the inlet side while only medium vacuum conditions exist on the outlet side.

The third pump used is an ion pump. The ion pump uses charged electrodes to ionise gas molecules, which are confined by a magnetic field until they are captured by another electrode. The pump does not remove the molecules in the same manner as a displacement pump so much as it condenses them onto a holding surface. Eventually the pump will need to be maintained by replacing or cleaning the collecting surface within it, as the contaminated surface reduces the pumps efficiency.

Another pump is occasionally used when a vacuum has been gradually contaminated by insertion and removal of other materials, the TSP (Titanium Sublimation Pump). This pump uses titanium as a getter to capture reactive molecules. The titanium, titanium-molybdenum alloy or in some cases tantalum, in the form of a filament or slug is heated to sublimation temperature, it then evaporates and deposits a thin film coating on the inside of the TSP chamber. The thin film is a fresh getter surface to react with a number of common reactive molecules. The getter's surface will need to be periodically replenished in order to maintain pumping efficiency. This type of pump can also capture hydrogen, the hydrogen does not react with the titanium but dissolves within the titanium bulk.

Another important pumping process is cryopumping. Cryopumping occurs when a surface inside the vacuum system is cooled below the temperature of the system during normal pumping. This process is not always intentional. Cryopumping has the effect of reducing pressure by cooling the gas molecules causing them to slow down, it also increases the probability that a molecule will condense onto a cooled surface when contact occurs. Cryopumping is not a permanent capture pump, when the temperature increases back to normal temperatures the molecules captured by this technique are usually released.

2.2.2 Bake-out

Baking out a vacuum system is one of the most effective methods of achieving UHV. The procedure involves increasing the temperature of the system so that the pressure inside is increased and the inner walls of the chambers out-gas any adsorbed molecules. This increased pressure is then sufficient to be pumped efficiently using turbo and ion-pumps. Once a stable low pressure is achieved at high temperatures (typically about 430-450K for the systems used in this research) the temperature can be returned to normal operating temperature. At the reduced temperature the pressure will reduce further than could normally be achieved within the same time without having increased the temperature. The surfaces within the vacuum system are also cleaner since the increased temperature has expelled some of the molecules coating them. The baking process can take a number of days to complete as the system needs to be heated evenly throughout in order to reduce any thermal stresses placed upon it and to allow time for the ion pumps to neutralise the increased pressure for each increment in temperature.

2.2.3 UHV Materials

All of the materials used in the construction and subsequent use within a UHV system must be UHV compatible. Some materials are unsuitable because they out-gas significantly or are adversely effected by the vacuum. The vacuum systems used in this research use carefully selected materials for the purpose of UHV. Stainless steel is used for the bulk of the vacuum systems construction. Glass port windows are used with specially strengthened glass able to withstand more than 1 atmosphere of pressure. Copper gaskets are used to seal the sections of stainless steel together, the copper gaskets are chosen as copper is a softer metal than stainless steel and the steel cuts a groove into the copper gasket to form a seal. This allows for a clean UHV seal without the use of possible contaminants such as rubber seals or vacuum grease. Once a copper gasket has been used and the seal re-opened the gasket must be replaced as the groove in the copper will not re-align once more with the edge on the steel sections. Other vacuum compatible materials include some ceramics (machinable ceramic) and some polymers often used for insulating wires. Certain materials are not suitable for UHV use. Aluminium is a metal which forms an oxide layer on it's surface, this oxide layer tends to gather a coating of gas molecules, this material out-gasses significantly while in

a UHV environment although Aluminium is suitable for HV use. Most porous materials are avoided for UHV work. Brass forms a porous oxide layer, which, collects gasses and other materials and out-gasses heavily in vacuum. All materials entering a UHV system need to be cleaned beforehand, this includes degreasing and the removal of any dust particles or foreign material.

2.3 Scanning Tunnelling Microscopy

The Scanning Tunnelling Microscope (STM) is a powerful tool for research into the properties of conducting and semiconducting material surfaces on a sub micron scale. It can provide topographical and electronic information from the material's surface and some electronic information from the near sub–surface.

2.3.1 History of STM

The use of quantum mechanical tunnelling as a tool for analysing the properties of materials is not a recent development. Early tunnelling experiments used insulating materials to form the barrier through which to tunnel[2].The tunnelling barrier was often formed by the controlled production of an oxide layer between layers of metal deposited by evaporation. Tunnelling was also observed in p-n junctions[3]. Indeed tunnelling is responsible for the current in a reverse biased low voltage Zener diode.

In 1981 Binnig and Rohrer *et al.* demonstrated tunnelling through a controllable vacuum gap[4] with the aim to develop a spatially resolved spectroscopic tool for electronic measurement of surfaces. In 1982 Binnig and Rohrer *et al.* report the first results from the first Scanning Tunnelling Microscope[5]. The basic function of the STM has remained largely unchanged since it's invention, however, there have been advances in vibrational decoupling and material technology which have made the system more reliable and capable. There have also been significant advances in computer technology and electronics that have facilitated automatic data collection and real-time signal processing as well as improving signal to noise ratios.

2.3.2 STM Theory

Scanning tunnelling microscopy is a probe microscopy in difference to conventional optical microscopy into which category visible light microscopes and electron microscopes fall. There is a fundamental difference in operation between optical microscopy and probe microscopy. Optical microscopy requires photons, electrons or other particles to be reflected from, transmitted through or produced by a target specimen and then collected by a lens and focussed into an image upon a collector. This image is interpreted as a facsimile to the original source enlarged by the magnification of the microscope. Probe microscopy differs in that the data produced is a measure of an

effect of a local interaction between the probe and the target specimen. The data can be collected at different points upon the surface of the specimen to form an image. The image produced by a probe microscope is not usually a visual representation of a material's surface but is a map of the specific interaction between the probe and the target specimen. In STM the probe is a conductor or semiconductor drawn, etched or otherwise formed into an apex tip. The tip is brought close to the surface of a conductor or semiconductor and an electrical potential difference is applied between them. When the probe tip is close enough to but not touching the target specimen electronic tunnelling will occur between the probe tip and the target specimen where there is a state of equal energy on each. In some situations there can be a net charge transfer from one material to the other and band bending occurs until the Fermi levels of each material match.

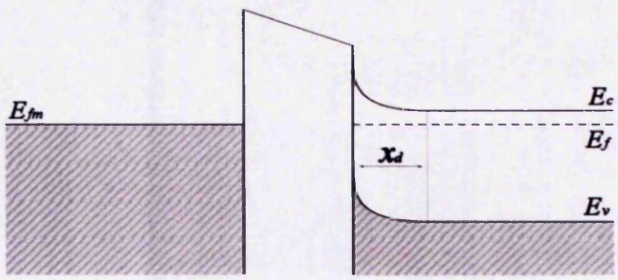

Figure 2.3.2-1: Metal and n-type semiconductor separated by a barrier. (thermal equilibrium).

Figure 2.3.2-1 shows a metal (left) and n-type semiconductor (right) separated by a barrier (vacuum gap) in thermal equilibrium, electrons have transferred by tunnelling from the semiconductor to the metal and brought the Fermi level of the semiconductor E_f and metal E_{fm} into equality. A depletion region from the barrier edge within the semiconductor of length X_d has been created. This region represents a bulk positive charge within the semiconductor. The equivalent negative charge for the metal remains on the surface of the metal as no bulk charge is allowed. In a p-type semiconductor the transfer is reversed and the electrons are transferred from the metal to the semiconductor.

If a potential difference V is applied between the two materials a current I is able to flow. The tunnelling junction becomes a charge transfer path. By varying the potential difference V and watching the effect on the current I, the local relationship between I and V can be observed.

2.3.2.1 Quantum Mechanical Tunnelling

Quantum mechanical tunnelling or tunnelling is a behaviour specific to quantum mechanics. If a particle in a classical mechanical system has not got enough energy to overcome a barrier it will not be able to traverse the barrier. This is not so for quantum mechanics, the position of a particle is a probability distribution given by its wavefunction. This wavefunction extends into and beyond the barrier, however, the probability distribution drops off as an exponential decay function through the barrier and so the probability is significantly reduced for most sizeable barriers so that the particle is largely confined by the barrier. In cases where the barrier is small enough tunnelling probabilities become significant. Tunnelling is an elastic process, there can be no energy lost or gained as a result of the tunnelling and so tunnelling will only occur between energy states that are equal. This leads to one of the most useful characterisation aspects of STM, the ability to map density of states by performing *I/V* spectroscopy.

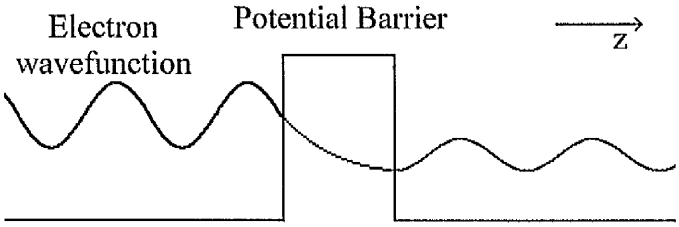

Figure 2.3.2.1-1: Electron wavefunction encountering barrier.

As with any circuit the current passing the vacuum junction between an STM tip and a sample material is dependant upon the impedance presented to the electronic potential difference by Ohm's law. That is not to say that the junction is Ohmic, it is not. There is a dependence of the tunnelling current on a number of parameters, the applied bias potential, the junction gap width, and the density of states (DOS) of the STM tip and sample materials. Binnig *et al.* proposed that the tunnelling current is given by the relationship,

$$I \propto e^{-A\phi^{\frac{1}{2}}d} \tag{2.1}$$

where I is the tunnelling current, d is the junction gap, φ is the tunnelling barrier height and $A=((4\pi/h)2m)^{½}$, where m is the free electron mass[5]. Other factors affecting the tunnelling include the tip morphology which was treated as being a locally spherical probe by Tersoff and Hamann which allows predictions to be made about the area of tunnelling beneath the tip[6,7]. However, this simplified model neglects effects brought about by realistic morphology such as kink sites causing local electric field

enhancement[8]. Lang expands on this concept in order to simplify the understanding of the basic concepts by modelling both the STM tip and sample as extended planar electrodes each with a single atomic protrusion[9]. The model of the STM tip as a hemispherical protrusion from an otherwise planar surface was used in a theoretical discussion by Bono and Good who introduce the WKB approximation for the tunnelling transmission probability[10] they expand this theory to include metal to semiconductor tunnelling[11].

2.3.2.2 STM: Modes of Operation

The STM can be operated in a number of different basic modes: constant height mode, constant current mode and a spectroscopic mode. In constant height mode the STM tip is brought close to the sample's surface (within tunnelling distance). The tip is then typically scanned in a raster fashion from point to point to form a grid. At each point the tunnelling current is measured for a fixed applied electrical potential difference. A data matrix representing the raster pattern and filled with the measured tunnelling currents for each respective point is produced. This matrix is the map of the tunnelling current and can be visualised by converting each measurement to an intensity value on a visual display unit. This method for STM scanning is very useful for studying the electronic properties of physically very flat (~1nm surface variance including roughness and slope) surfaces in a vibration free environment. This technique is not useful when vibrations, significant topography, or an otherwise uneven surface is present.

The most commonly used mode of operation of the STM is constant current mode. In constant current mode the tip is positioned within tunnelling range of the sample's surface. With a constant applied electrical potential difference between the tip and sample a feedback loop is engaged. The feedback loop causes the separation of the tip and sample to be adjusted automatically to maintain a specific tunnelling current (the current set point). The tip is then scanned in a raster fashion, as with constant height mode, and measurements taken to fill the representative data matrix. In difference to constant height mode the data collected in this mode is the output of the feedback loop used to keep the current constant. The output of the feedback loop is usually a voltage applied to a piezoelectric motor which adjusts the position of the tip relative to the axis normal to the sample's surface (the tip sample separation) d. The image produced from the data matrix uses intensity to represent Z position of the tip. This method for STM

operation is capable of tracking the surface of a metal or semiconductor over a large *Z* range (200nm has been achieved with the systems used in this research).

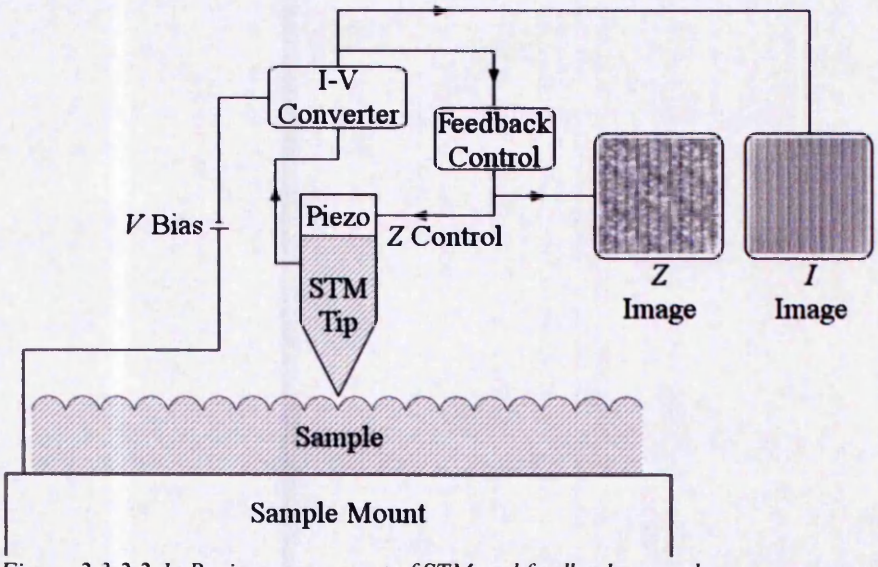

Figure 2.3.2.2-1: Basic arrangement of STM and feedback control.

Figure 2.3.2.2-1 shows the basic arrangement of an STM including the feedback control. When in constant current mode the *I* image as depicted in figure 2.3.2.2-1 shows any deviation from the set point due to changes in current that can not be compensated for by the feedback loop, this can include high frequency vibrations and large surface features. When the feedback loop is disabled or is operating with very little effect the *I* image represents the surface topography and electronic information.

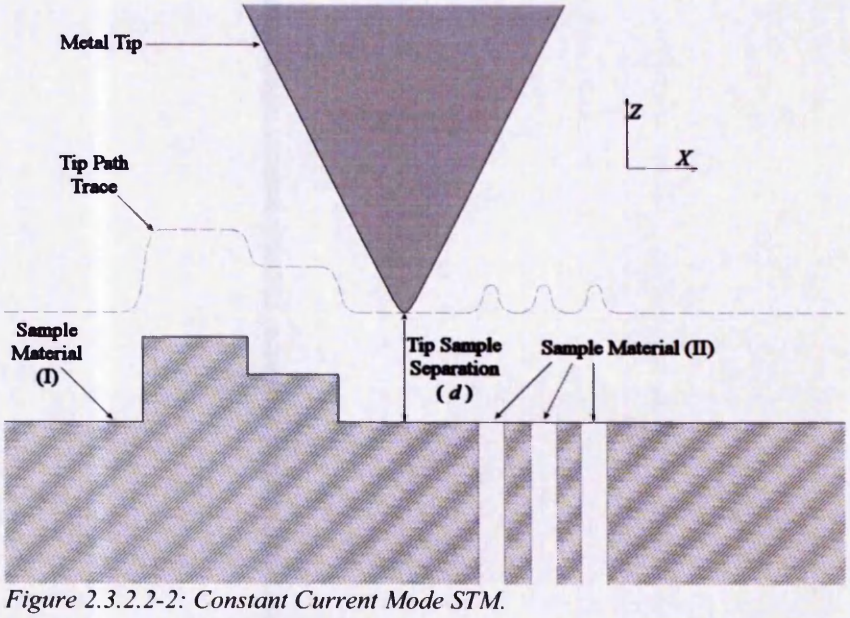

Figure 2.3.2.2-2: Constant Current Mode STM.

Figure 2.3.2.2-2 shows an STM operating in constant current mode. The STM tip is

scanned in the *X* direction while the feedback loop adjusts the tip's position along the *Z* axis. Topographical features shown in the left of figure 2.3.2.2-2 are traced by the tip so that a constant current is observed which leads to a near constant tip-sample separation *d*. When the STM tip moves over the region of different electronic structure, such as the region with different chemistry in the right of figure 2.3.2.2-2 the current will tend to change away from the set point and so to compensate the feedback loop adjusts the tip-sample separation *d*. Both topographical and electronic information are convoluted in this regime.

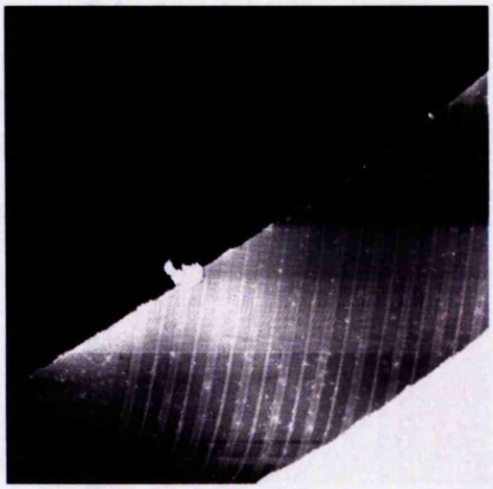

Figure 2.3.2.2-3: Electronic and topographical information.

Figure 2.3.2.2-3 shows combined electronic and topographical features. A quantum well structure (vertical stripes) competes with topographical steps (diagonal partitions). The surface topography washes out the electronic information in this case.

The tip path trace as shown in figure 2.3.2.2-2 does not follow exactly the features on the surface, there is a slight smearing effect of the edges of the topographical and electronic information. This smearing is caused by the profile of the STM tip and the response of the feedback loop, a very sharp tip will keep this effect to a minimum and a faster feedback loop response time will also reduce this effect, however, it remains present. If the feedback response is too fast ringing (overshoot) and oscillations can occur. There are signal post-processing methods available to enhance images and reduce the appearance of the smearing effect.

Various methods are used to discriminate between topographical and electronic information, and are utilised depending upon the specific materials and electronic structure present. By varying the electrical potential difference between the tip and

sample, different tunnelling states can be selected, some states will promote electronic structure imaging and others will diminish it. Changing the polarity of the tip-sample potential difference is often an effective method.

The STM facilitates localised electronic spectroscopy to be performed along with other measurements. The probe tip can be positioned so that tunnelling occurs within a region of sub-nanometre scale below the apex of the tip. This allows for detailed electronic information to be gathered by varying the electrical potential difference V between the tip and sample while measuring the effect on the current I. The I/V relationship can be used to investigate the Local Density Of States (LDOS) of a material and tip and aid in the visualisation of the material's band-gap. These spectra can be collected at multiple positions on a material's surface to produce a map of the electronic properties. A single STM data set from constant height mode of operation can be considered to be a slice through an electronic spectrum data set over many locations on the material's surface. A similar interpretation may be held for constant current mode, however, Z effectively replaces I in this case.

Noise caused by electronic and mechanical sources and other instabilities can cause errors in the spectrum collected. The effect of noise can be dramatically reduced by taking a number of spectra and averaging the set, this can be done on a single location on a material's surface or an average over a region can be produced. This latter method can also reduce the effect of very localised anomalous spectra on the resultant data set.

2.3.2.3 STM Materials

STM is a very precise microscopy, able to scan areas from a few square microns to a few square nanometres and maintain relative accuracy across the whole range. The Z control is required to maintain a tip sample separation d of ångströms over a Z range of about a micron. There must also be coarse positioning control to enable macro scale selection of sample region and to approach and retract the probe tip, both of these must be able to operate over the millimetre range. The Z coarse control over a few centimetres in range may be required to manage various sample configurations. The dynamic range of positioning required is very high. Piezoelectric motors are able to satisfy both the coarse and fine positioning control. A set of slip-stick motors are able to move the sample laterally along both the X and Y axes at least over a range of a few millimetres and usually into the centimetre range. The Z slip stick motor is able to

control the tip position over a few centimetres range using up to 1 micron step sizes. These motors use the inertia of their load to facilitate their function. The slip stick motor as its name suggests engages and disengages two surfaces with friction and inertia respectively. The piezoelectric material engages a supporting surface and extends gradually to reach maximum length, the signal used to extend the material is then cut rapidly and so the material returns to its natural length rapidly. The inertia of the load supported by the motor is too great to accelerate and so the piezoelectric material slips across the supporting surface and the cycle is repeated. By changing the waveform of the controlling signal from a left hand sawtooth to a right hand one the motor can change direction. Another piezoelectric motor is able to perform this task, the inchworm motor, however, it is not used in this research. The inchworm motor has a set of three piezoelectric actuators in a linear formation, the first and last can clamp to the supporting material when a voltage signal is applied, the middle actuator can change the separation of the first and last actuators. By selectively engaging one of the end actuators and extending the middle actuator before engaging the other end actuator and releasing the first then contracting the middle actuator the inchworm will travel along the supporting surface, continuous repetition of this process gives this motor a virtually unlimited range.

The fine tip control used for scanning is usually a piezoelectric tube referred to as the scanning tube. The tube usually has at least five electrodes to control it. One earth electrode in the centre of the tube and four electrodes spaced at equal separation around the tube and extending nearly the entire length of the tube. With these electrodes and suitable mixing circuitry it is possible to produce controlled motion along all three axes independently and simultaneously.

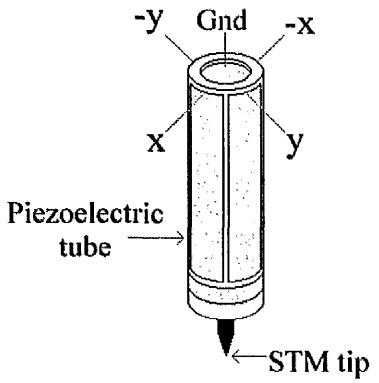

Figure 2.3.2.3-1: Piezoelectric scanning tube.

Figure 2.3.2.3-1 shows the configuration of a typical scanning tube. The configuration here is the same as that used in the Low Temperature STM (LTSTM). The room temperature STM has the sample mounted on the scanning tube and the STM tip is fixed. Generally the STM tip is referred to as scanning across a sample's surface, the latter being the fixed point of reference, however, both combinations are used. In some rare cases both the STM tip and the sample are mounted on scanning tubes, the primary advantage to this is that the *X*, *Y* and *Z* signals do not have to be mixed. In order to move the STM tip along the *X* axis alone equal signals with opposite polarity are applied to the x and -x electrodes. The same procedures applies to the *Y* axis. To facilitate *Z* motion an equal signal of the same polarity is applied to the x, -x, y, and -y electrodes. The separation between electrodes is of the order of a millimetre and the signals used to drive them can range from millivolts to over one hundred volts and so the piezoelectric transducers should only be used at high pressures (atmospheric) or UHV pressures to avoid an arc discharge with low pressure gasses.

Piezoelectric motors require contamination free surfaces on which to travel, contamination and debris can impede their operation severely. The response from a piezoelectric actuator is temperature dependant and so the control unit needs to be calibrated to the working temperature.

Piezoelectric materials have a hysteresis associated with their operation. If a constant voltage signal is applied to a piezoelectric motor to move it it will deform as would be expected, most of the deformation process would take place within a short time period and the remaining deformation (creep) motion will occur more gradually over an

extended time period. This leads to a number of issues and considerations with respect to STM. If an offset is applied to the scanning tube and scanning commenced the region scanned by the tube will change slowly during the scan. It can, in fact take many scans to make this drift effect negligible. Figure 2.3.2.3-2 shows both drift during and drift between a sequential pair of STM scans. A set of features have been highlighted to show this. The orientation of the scanning vector is intended to be orthogonal to (*X*) and parallel to (*Y*) the quantum wells in these images, the continuing creep from the piezoelectric tube is effectively skewing the scanning vector.

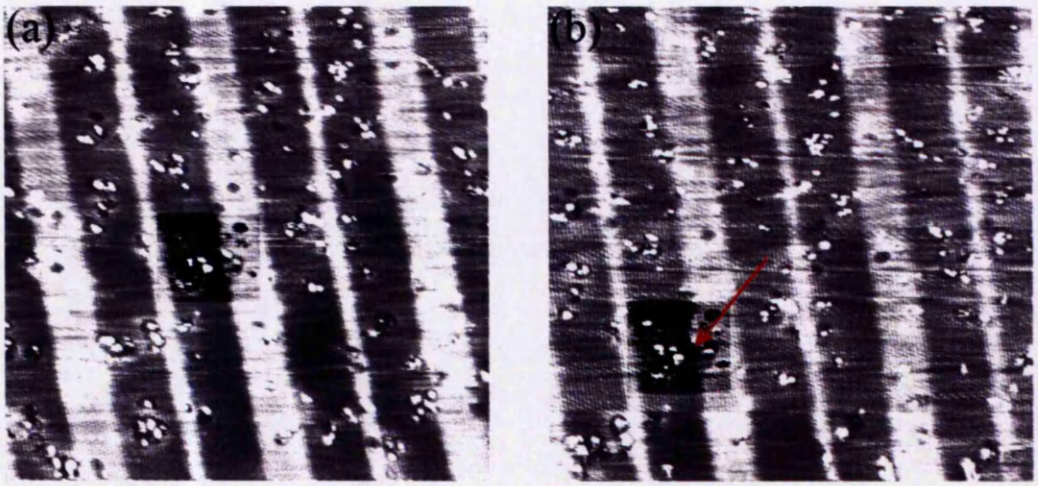

Figure 2.3.2.3-2: Sequential scans showing X-Y drift of STM tip in operation.

This effect is also apparent when the size of the scan area is changed without changing the offset. The rate of this relaxation process is temperature dependant. Another source of drift is thermal changes within the system. It is normal to allow an STM to scan a region a number of times before collecting data to reduce the drift in the collected data. Lateral drift in the *X-Y* plane can be compensated for by subsequent data manipulation if the rate of change of drift is low over the course of one scan. This is performed by artificially readjusting the scanning vector by data post processing. The drift effect is not a significant problem with *Z* motion in constant current mode operation as the feedback loop adjusts the position to maintain a constant current. It will lead to some sloping of the data once collected, however, this is usually not on a length scale that will affect the results if removed from the data after collection. Removal of surface slope and *Z* drift is a routine procedure. In constant height mode operation drift of the *Z* position is a significant problem, in order to collect data reliably the drift must be negligible.

A number of techniques are available to remove surface slope from collected data, the simplest involves subtracting the end to end gradient of each scan line from the data which is effective for a linear surface slope, however, this technique can introduce bowing in the data if the underlying slope or apparent slope is not linear. More involved slope correction methods include the removal of low frequency components from a Fourier analysis of the data or the subtraction of two dimensional polynomial surface slope models. As with all Fourier analysis the introduction of ringing artefacts in filtered data is undesirable.

Mechanical isolation is an important consideration within a STM's construction. A tip-sample separation d of ångströms can be adjusted significantly by relatively small vibrations in the air or supporting surface. The vacuum commonly used with STM eliminates acoustic vibrations from affecting the tip-sample separation. In some cases it is necessary to operate the STM at atmospheric pressure, in such cases normal sound levels including speaking and sound from mechanical sources can affect the tip-sample separation. Simple acoustic shielding can significantly reduce this effect. Transmission of mechanical vibrations through the supporting structure can be controlled by careful design. The original STM produced by Binnig and Rohrer *et al* floated the STM head and carriage on a magnetic levitation platform[4] this arrangement utilises the inertia of the carriage to transfer vibrational energy into the magnetic field supporting it, the energy is eventually released by inducing eddy-currents in a sheet of metal in the vicinity of the magnets. The systems used in this research both use long springs to support the STM head and carriage. The carriages have copper radial elements which are lowered along with the carriage into a ring of permanent magnets in an alternating field polarity configuration. This approach causes rapid damping of mechanical vibrations by converting the energy, via eddy-currents, into small increases in the temperature of the copper radial elements.

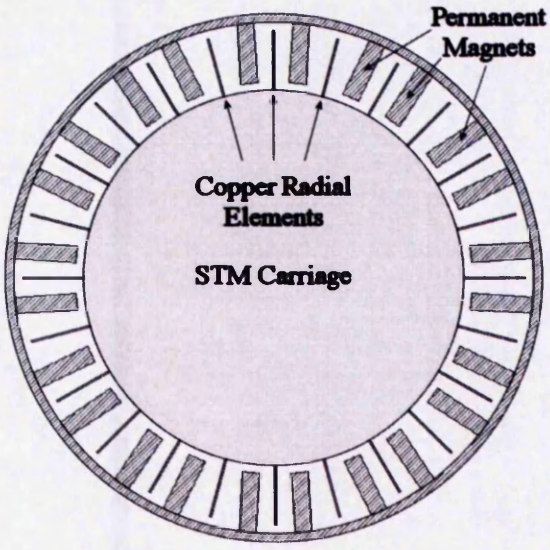

Figure 2.3.2.3-3: Plan view of STM carriage lowered into ring of permanent magnets.

The magnetic dampening system is effective at preventing high frequency vibrations from reaching the STM carriage and the spring suspension and inertia of the STM carriage is effective at preventing lower frequency vibrations from reaching the carriage. Thin copper wires long enough to allow for movement are used to make the necessary electrical connections to the STM head while traversing the anti-vibration system and transmitting minimum vibrational energy. A further anti-vibration system is employed to impede building vibrations entering the system. The entire STM, vacuum chambers and operating bench are mounted on inflated rubber supports.

2.3.2.4 Low Temperature STM

In some situations it may be necessary to perform STM and associated techniques at low temperatures. Most materials exhibit different properties at different temperatures, semiconductors and nano-structures are no exception. Semiconductors used in many electronic applications use thermally excited carriers, which change in number with temperature. Some thermistors are semiconductor devices which makes use of this effect. The ability to perform STM at different temperatures enables the investigation of these properties or other phenomenon that are affected directly or indirectly by temperature.

The LTSTM (Low Temperature Scanning Tunnelling Microscope) is a STM configured for use at low temperatures, the LTSTM used in this research has been designed to incorporate a cryostat for use at liquid nitrogen and liquid helium temperatures, 77K

and 4K respectively. The LTSTM can be cooled by either filling the cryo-baths with liquid nitrogen and refilling when necessary or by operating in a continuous flow regime whereby the inner bath is continually replenished with the specific coolant. Heat is transferred away from the tip and sample by two paths, one is a direct physical contact with a cold surface behind the sample, this method is used for initial temperature reduction or intermediate cooling. The sample and tip in their carriage is lifted into direct contact with the cold surface. Stable tunnelling is not achievable during this cooling as the anti-vibrational system is bypassed. The secondary heat transfer route is a constant cooling method based upon a braided copper wire thermal contact which has enough freedom of movement not to transmit significant levels of vibrational energy. Surrounding the entire carriage is an interlocking heat shield. The gold coated heat reflectors have quartz windows to allow the passage of visible light during use. The interlocking heat shield can be arranged to allow light through or not at all. An internal thermometer is positioned directly to the rear of the sample mount and can measure the temperature accurately to within ±1/10K.

A side effect of low temperature STM is cryopumping. During use at low temperature the pressure within the STM chamber drops as thermal energy is removed from the remaining gas molecules and some are condensed onto surfaces within the vessel. One undesirable effect is that condensates and adsorbates condense and adsorb onto the surface of the sample being studied. The level of condensates and adsorbates increases over time as more and more material is captured, this reduces resolution on the surface and can actively interfere with electronic imaging and spectroscopic measurements while adding topographical features. The piezoelectric tube and motors operate over a significantly reduced range at 77K and 4K and so the controlling system is calibrated to maintain spatial accuracy. The motors are also affected by condensed materials on their surfaces.

2.3.2.5 Cross Sectional STM

The X-STM (Cross Sectional Scanning Tunnelling Microscopy) technique varies from normal mode STM in one fundamental way, the sample is mounted in the STM so that the tip can scan laterally along the axis of epitaxial growth of the sample. This requires the sample to be mounted vertically within the STM system and cleaved to present a clean flat surface to the STM tip. The tip is positioned over the epitaxially grown structure and scanned to produce cross sectional images of the epitaxially grown structure. X-STM allows spatial characterisation of epitaxially grown structures and devices as well as detailed electronic investigations of their properties. Feenstra *et al.* demonstrated '*atom-selective imaging of the GaAs(110) surface*' whereby an *in situ* cleaved (110) surface of GaAs was presented to the STM[12]. Spectroscopic techniques were used to identify and individually image either Ga or As atoms.

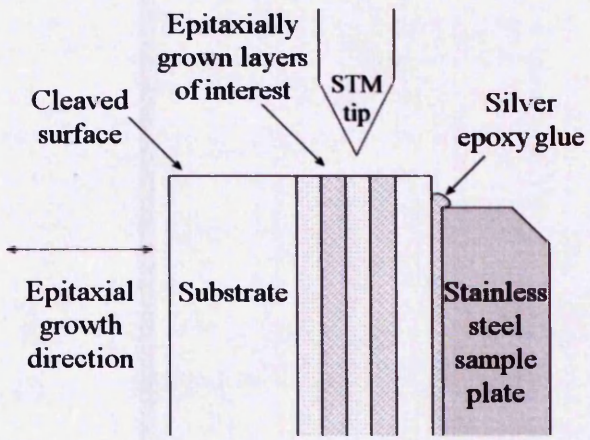

Figure 2.3.2.5-1: Cross sectional STM arrangement.

Figure 2.3.2.5-1 shows a typical cross sectional STM arrangement with a sample material glued to a stainless steel sample plate using silver loaded epoxy glue. In this figure the materials top surface is glued to the sample plate, however, the substrate may be mounted on the sample plate also. The former arrangement is that used in this research. One of the greatest advantages of cross sectional STM is the clean nature of a freshly cleaved surface. By transferring a material from a growth reactor into an STM directly through vacuum, a similarly clean epitaxial surface can be investigated. Without using either of these methods the only way to access a clean surface is to clean it.

2.3.2.6 Photoenhanced STM

Photoenhanced STM covers a wide variety of techniques with which STM investigations are complimented and enhanced by the simultaneous measurement of the effect of light on or detection of light produced by the system being investigated, or occasionally, both.

In these investigations the photoenhanced STM employed is the former, the sample material is illuminated in order to study the effects of this illumination on its electronic characteristics.

There are a number of photoenhanced STM modes of operation used in this research. By simply shining a broad spectrum light source, such as that produced by an incandescent (halogen) lamp, on to the sample and monitoring the effect this has on the tunnelling current at various points of interest over the material's surface in comparison to no applied light and possibly a variable intensity light source. The light may excite the material in a number of ways. The light will thermally excite the material possibly causing a measurable thermal expansion, the light will also excite electrons between energy levels in a direct band-gap material causing electron-hole pairs. van de Walle *et al.* utilised the effects of light from an incandescent halogen lamp and a 5mW He-Ne laser to excite carriers in semi-insulating (SI) GaAs in order to enable STM studies of its surface. The light excited electron-hole pairs in the material enabling current to flow[13]. This process will also occur in indirect band-gap materials where thermal energy can provide the necessary momentum vector in k-space to make a direct transition. Where there are quantum well or quantum dot structures in the material the light may excite electrons into confined electron-hole pairs. By using a specific wavelength of light it is possible to target specific transitions in the material such as a specific quantum well energy gap. The benefits of using a single wavelength light-source such as a laser or a broad spectrum light source passed through a monochromator is that individual features can be tuned-in to without exciting everything else, and that the necessary wavelength of light can be used to excite a specific transition without causing unnecessary heating of the material caused by the unused energies from a broad spectrum light source.

Thermal excitation of the material and of the STM tip is a problem for photoenhanced STM. The tip and sample may expand or otherwise deform when exposed to a broad

spectrum or laser light source, this will affect the tunnelling gap between the tip and material sample. If the illumination is constant throughout an experiment using constant current mode STM the feedback loop will readjust the gap automatically until thermal equilibrium has been achieved. If, however, the light intensity is varied as part of the experiment or through other means during the experiment the intensity change will cause a change in the tunnelling conditions during an experiment and could invalidate the results. Amer *et al.* utilised this photothermal effect to modulate the tunnelling gap between the tip and material sample within an STM with the intention of measuring the material's work function[14]. They describe the modulated laser source as buckling the sample material's surface by up to 1Å, and seem to completely ignore the effect of the laser light source on the STM tip. The dimensions of the STM tip at its apex are such that even a modest light source would have a significant effect on it, causing a measurable extension often more significant than that of the sample. Grafström *et al.* demonstrated the significance of the effect of photothermal excitation on the STM tip and identified the component relationship between light pulse frequency and photothermal expansion response[15]. It is also important to maintain a stable operating temperature for STM to reduce the effect of thermal drift on the region being investigated.

Another technique used in this research is locked in photoenhanced STM. This technique uses a Lock In Amplifier (LIA) similar to that used in AFM non-contact mode of operation and various optical spectroscopic techniques. A light source such as a laser is pulsed so as to produce a temporal pulse train of light incident upon the material sample's surface. A voltage signal in phase with the pulses is used by the lock in amplifier as a reference signal. The voltage signal is usually generated by the system pulsing the light source such as a chopper, acousto-optic modulator or a simple oscillator controlled power supply. The latter only applies to incandescent light sources and semiconductor based light sources such as LEDs and LDs. The STM tunnelling current signal is input to the lock in amplifier. In this configuration the STM is operated as normal, however, the output of the lock in amplifier is also monitored. The output from the lock in amplifier is a voltage signal that depends upon the frequency component of the STM tunnelling current that is in phase with the light modulation. The result is a second signal that can be monitored and mapped alongside a normal STM *I* or

Z scan, this signal shows only the part of the tunnelling current that is directly caused by the interaction of the light and the material. It is, therefore, possible to map photosensitive regions of the material's surface independently of other information including surface morphology, external sources of vibration and other electronic information. The light modulation frequency must be high enough to be filtered out by the *Z* feedback response and to allow surface features to be resolved as the tip passes over them in a finite time. Some one-shot features such as topographic steps have broad frequency components and so may be detected by the lock in amplifier as a transient signal. Such information will filter through the lock in amplifier and be presented as a value on the output.

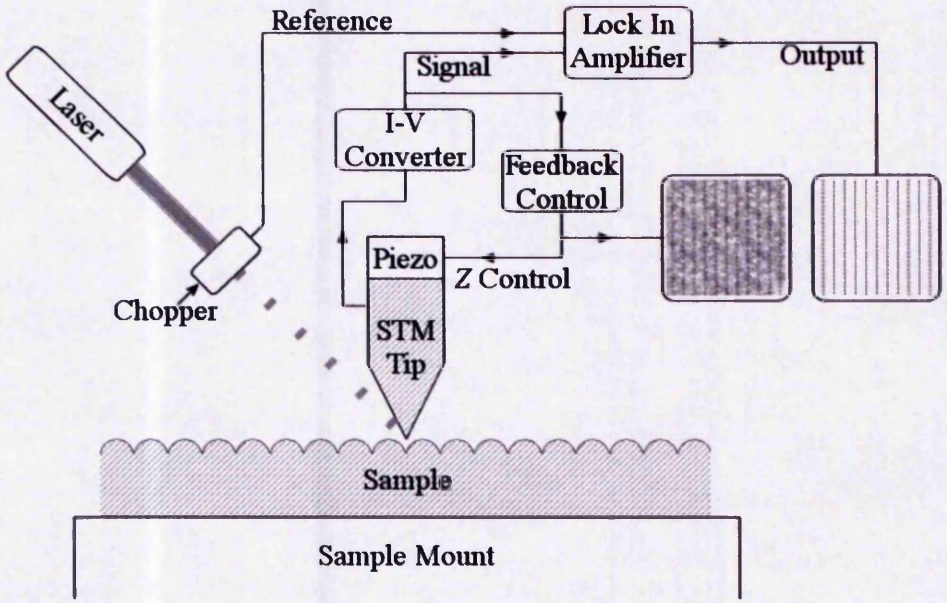

Figure 2.3.2.6-1: Arrangement of components in locked-in photoenhanced STM.

Figure 2.3.2.6-1 shows the arrangement of the STM system and lock-in amplifier for use in locked-in photoenhanced STM, this arrangement was used in this research.

The lock in amplifier operates by effectively multiplying the two input signals together both the reference and the experimental signal. The result of multiplying two signals together is the sum and difference frequency signals. Since the resultant component of the experimental signal is the same frequency as the reference signal (assuming there is a component) the difference frequency signal is zero. The result is a DC signal proportional to the component of the experimental signal at the same frequency as the reference signal and is proportional to the cosine of the phase difference between the

reference signal and the same frequency component of the experimental signal. A phase shift can be applied to the reference signal to reduce the phase difference to zero. The end result is a DC level signal dependant upon the signal component of the experimental signal that is both in phase and frequency matched to the reference signal. A time based low pass filter is usually the last phase of the processor, this filters out noise components of the input signal that are in phase by effectively time averaging. Most modern lock in amplifiers are implemented in digital electronics using sophisticated high speed DSPs (Digital Signal Processor). Setting the parameters of the lock in amplifier is a compromise between signal response time and accuracy (signal to noise ratio). In order to increase accuracy in some cases the experiment can be slowed down allowing for greater time averaging between measurements.

2.4 Atomic Force Microscopy

2.4.1 Introduction to AFM

AFM (Atomic Force Microscopy) is very similar to STM in operation this allows the construction of a dual AFM/STM system possible. The difference in operation lies in the probe sample interaction. While STM uses quantum mechanical tunnelling to investigate the electronic and topographical properties of the sample, AFM uses the attractive and repulsive van der Waals forces between atoms to investigate the topographical features of material surfaces.

The forces experienced between the probe and tip can be measured in a number of different ways, the AFM used in this research uses an infra-red LD (Laser Diode) to position a spot of light onto the back of the AFM cantilever. As the probe experiences force the cantilever is deflected from its relaxed position according to Hooke's Law and the angle of the reflected light changes. The degree of deflection of the cantilever can then be monitored by a quadrant photodetector.

The technology behind the STM gave rise to the AFM in 1985, Binnig *et al.*, the original inventors of the STM, developed a method for sub-nanometre investigation of the topographical features of insulating materials[16]. The AFM is conceptually an extension of the stylus profilometer down to sub nanometre scales, a lateral resolution of 30Å is reported using the original AFM[16]. This original AFM used an STM to measure the deflection of the AFM cantilever. The probe was a diamond tip mounted on one end of a gold foil 0.25mm wide and 0.8mm in length. This apparatus was operated in a variety of modes which all roughly approximated modern non-contact mode AFM. Advancements in deflection detection and probe production since the original invention enabled the direct contact mode AFM.

AFM has facilitated a new region of nano-scale investigation, where previously topographical images were limited to conductors and semiconductors, it is possible to get direct topographical imaging of any material that provides an inter-atomic (van der Waals) forces of attraction and repulsion including solid insulators and non-insulators, the surfaces of liquids and biological matter. The latter notably includes the DNA molecule, protein molecules and living cells.

Another result of the ability to measure the minute forces deflecting a cantilever is the

development of microscopies based on other forces such as MFM (Magnetic Force Microscopy) and the KPFM (Kelvin Probe Force Microscope).

The two most common modes of operation of the AFM are contact mode and non-contact mode.

2.4.2 Contact mode AFM

Contact mode AFM is one of the most commonly used modes in modern AFM. The relative simplicity of this method makes it the natural choice for preliminary investigations of solid surfaces.

In contact mode AFM the probe tip is brought close to the material specimen being investigated. Within a few ångströms of the atoms of the target sample; the probe tip, as does the sample's surface, experiences an attractive force between them. When the probe tip is brought even closer this force will become repulsive. Both the attractive and repulsive forces cause a deflection on the cantilever in accordance with Hooke's law, which can be measured by the transducer employed to detect this. Contact mode AFM relies on absolute measurement of cantilever deflection, since a stationary probe in contact with a surface experiences a constant force. The AFM used in this research uses a laser and quadrant photodetector to detect this deflection as shown in figure 2.4.2-1. A feedback loop is used to maintain a constant predetermined force between the probe tip and sample by adjusting the Z position of the sample with respect to the probe tip based upon the offset detected by the photodetector.

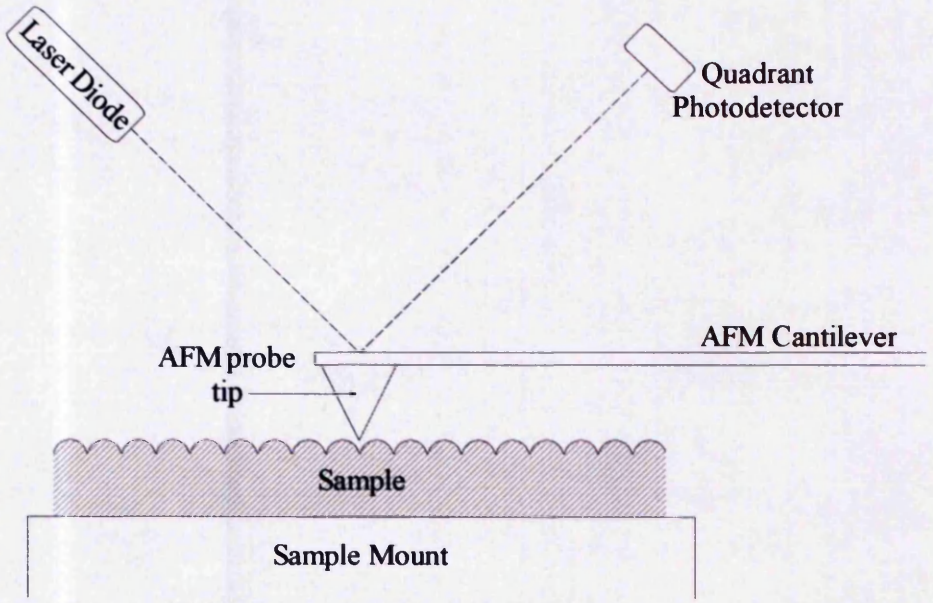

Figure 2.4.2-1: AFM probe arrangement used in this research.

Figure 2.4.2-1 shows a typical AFM experimental arrangement, light emitted from the laser diode is incident on the back of the AFM cantilever. The reflected light is detected by a quadrant photodetector. Any deviation of the cantilever from a zero position is detected. In this figure no force is acting on the probe tip. There may be a set of mirrors to aid in positioning of the laser light upon the cantilever and subsequent targeting of the reflected light onto the quadrant photodetector. In this case these procedures are performed when no force is present on the cantilever.

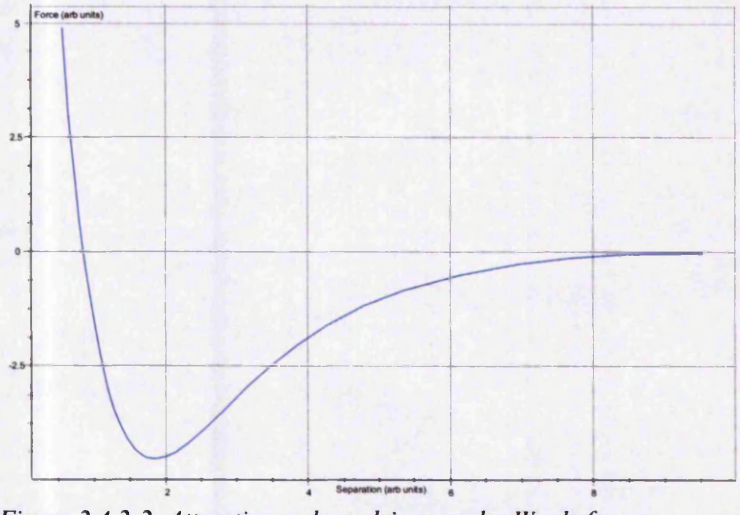

Figure 2.4.2-2: Attractive and repulsive van der Waals forces.

Figure 2.4.2-2 shows a graph of the van der Waals forces between unbonded atoms, the attractive force regime exists to the right of the graph (all regions below y=0) and the

repulsive force regime exists to the left of the graph (all regions above y=0). Where y=0 the force is neutral and two atoms are stable at this separation. The dip in the graph is a result of the competing attractive and repulsive forces.

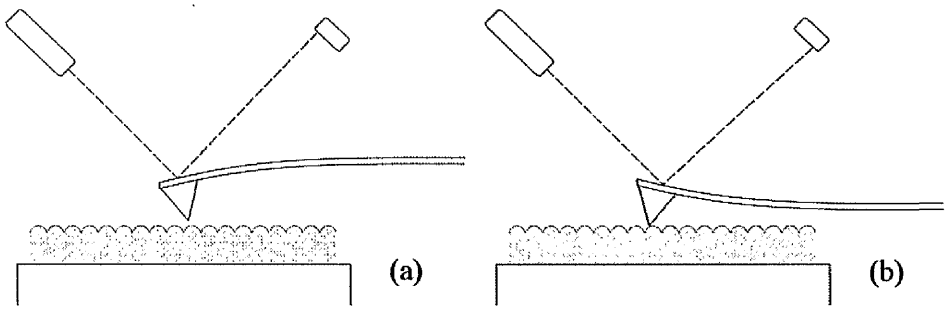

Figure 2.4.2-3: AFM cantilever deflection during attractive (a) and repulsive (b) forces.

Figure 2.4.2-3 shows the deflection of the cantilever during attractive and repulsive forces and their effect on the path of the laser light. The attractive regime (a) corresponds to the regions in figure 2.4.2-2 below y=0 and the repulsive regime (b) corresponds to the regions in figure 2.4.2-2 above y=0. Lateral and torsional forces can also be measured giving rise to TFM (Torsional Force Microscopy). Contact mode AFM makes use of the repulsive force regime (the region above y=0 in figure 2.4.2-2), although the same technique can be used in the attractive regime this non-contact method is usually not stable as the probe may lose the attractive force by either increased or decreased *Z* motion and so the feedback control system has no definite response that will compensate for the deviation from the set force. If the system was in constant height mode in the attractive regime the probe tip is probably going to lose attractive contact entirely and thus move away as the cantilever relaxes, and not regain this attractive force until a prominent feature reclaims it. The result is an intermittent probe- surface interaction.

Once the set force (usually measured in nano-Newtons) has been achieved the probe tip or sample is scanned in a raster pattern forming a matrix, the matrix elements are the *Z* values from the feedback loop required to keep the force constant. Lateral values can also be measured and entered into another matrix, this can often give information about the path of an AFM probe over a feature. Occasionally when imaging at the edge of a steep feature probe tip may move laterally around the feature instead of over it, this data can reveal if this has occurred. The raw deflection data from the quadrant photodetector can be used to judge the effectiveness of the feedback loop to maintain constant force

and hence constant deflection. In some situations when vibrational energy from an external source is present the feedback loop can be adjusted in order to not respond to the vibrations, in which case they will appear on the raw data from the quadrant photodetector since they are not compensated for.

Contact mode AFM can be operated in a similar mode to constant height mode STM. If the feedback loop is disabled and the probe sample separation fixed the probe can be scanned at a constant height. The data collected in this mode of operation is the raw deflection of the cantilever as measured with the quadrant photodetector. As with constant height mode STM this can only be performed on very flat samples. Rough or sloping samples could damage the probe tip, the sample or both and in some cases the cantilever can be broken.

The proximal nature of contact mode AFM has advantages and disadvantages. In some situations a layer of water vapour will condense onto the sample being investigated, a contact mode AFM probe tip will initially be attracted by the thin water film, however, it will penetrate the film and reach the sample before the repulsive regime exists. Contact mode AFM, therefore, is capable of operating irrespective of moisture on the sample's surface. This same proximal nature and the forces it entails, hails some less desirable effects in the field of material characterisation, the forces between the probe tip and sample are great enough to interfere with the probe tip, the sample or both. It is common for contact mode AFM tips to wear out after some use. This wearing process can deposit material from the tip onto the sample's surface, contaminating it. The tip can in the same way damage the sample's surface causing indentations or gouges, this may be a negative issue for characterisation, however, it is also a method of nano-indentation or nanolithography. Depending on the hardness of the materials composing the sample and tip one may be damaged before the other. This is especially true for soft materials or samples of biological origin. Silicon, from which the AFM probes are produced has a Mohs hardness of approximately 7. Another consideration is the electrostatic charge that can be created between the probe tip and certain material samples, caused by the friction of dragging the tip over the sample's surface.

2.4.3 Non Contact mode AFM

NC-AFM or Non Contact mode Atomic Force Microscopy is the mode of operation associated with the original AFM[16]. NC-AFM operates in the attractive force regime of the van der Waals force (below y=0) curve in figure 2.4.2-2. During operation the cantilever deflection enters the regime shown in figure 2.4.2-3a. The probe-sample separation in this regime is typically tens to hundreds of ångströms.

During operation the AFM probe cantilever is physically vibrated near its resonant frequency of oscillation in the transverse direction (*Z* direction in SPM topology) by a piezoelectric motor supporting the probe. When the probe tip is free the probe's natural resonant frequency and amplitude will be expressed. If the probe tip is brought close to the sample material's surface the attractive force experienced by the probe tip will augment the natural resonant frequency of oscillation and act to dampen the oscillations and shift the resonant frequency. This shift in resonant frequency is a measure of the probe-sample interaction. By setting the feedback loop to adjust so that the resonant frequency is set to a constant shift from free resonance the probe will maintain a constant attractive force upon closest approach with the sample.

A lock in amplifier is used to separate the signal related to probe-surface interaction effects from other detected signals and compare the augmented resonant frequency with the free natural resonant (driving) frequency. The output from the lock in amplifier is a changing DC (Direct Current) voltage signal proportional to the difference in phase, amplitude or more commonly frequency of the two signals. The lock in amplifier is very sensitive to small signals at a specific frequency. NC-AFM makes use of this feature since the van der Waals attractive force is considerably smaller than the repulsive force used in contact mode AFM. The output from the lock in amplifier is used as the input to the feedback loop.

During operation the probe is scanned in a raster pattern over the material's surface and the resultant *Z* motion of the probe is the value measured and entered into the representative data matrix.

The probe used for NC-AFM differs from that used for contact mode AFM, it typically has a shorter and stiffer cantilever which has a much higher resonant frequency (100-400kHz). To maintain a single strong resonant mode the cantilever is only produced in the mono-arm type, the dual-arm variety as depicted in figure 2.5.2-1 is not suitable for

this mode of operation.

A number of differences in measurement arise from the differing modes of operation of AFM and NC-AFM. If a material is free from moisture or other liquid media on its surface an image produced by NC-AFM may be very similar to that produced by contact mode AFM. However, in the presence of a surface film of water the NC-AFM probe will rise over the moisture and image that instead of the material's surface beneath it. Heat treatment of some samples may remove the moisture layer in vacuum or very dry ambient conditions. This effect is not always unwanted however, the ability for the NC-AFM to image wet environments has allowed it to play a central role as an instrument for microscopy and measurement of biological and other soft or liquid materials. The main advantage of NC-AFM is it's non intrusive imaging capacity. NC-AFM probe tips experience little or no friction or contact with the materials they image, this leads to a very long operating life for the probes in comparison to contact mode AFM. The probes, therefore, do not contaminate or otherwise interfere with the materials they image, this is advantageous when imaging delicate electronic structures or living cells.

A variation on this mode of operation is tapping mode AFM or intermittent contact mode AFM (IC-AFM), in this mode the extreme point of a single vibrational period of the AFM probe tip towards the sample enters the contact mode regime of repulsive force. The advantages to this mode are the ability to perform contact mode AFM type measurements without the associated frictional damage to the tip and sample, or electrostatic charge caused by dragging the tip over the sample's surface. This allows contact AFM type measurements to be performed on soft or fragile sample materials.

2.5 Tip and Sample preparation

Both the STM tip and sample need to be prepared in a suitable manner prior to investigation within the STM. AFM tips may also be augmented to suit their specific purpose.

2.5.1 STM Tip Preparation

The STM tip needs to meet certain physical requirements. It must be conducting or at least semiconducting, it must narrow down to an apex point with ideally one atom at the very tip and it must be stable within the preparation and operating environments in which it is used. The original STM used tungsten (W) tips produced by grinding down 1mm diameter wire, this crude approach to tip production had great success when combined with a soft crashing tip preparation on the sample's surface could produce tips capable of resolving mono-atomic steps with a resolution of 10Å[4-5]. It is worth noting that techniques used to produce STM tips historically have been a direct extension of those used for the production of field emission microscopy tips, however, the increased resolution requirements and decreased size scales has required considerable refinement to these techniques. Most STM tips are composed of metals, either elementary or in alloys. The most common metal for use in STM tip manufacture is tungsten, it is a hard metal which is stable over a wide temperature range and is relatively unreactive. Tungsten forms a protective oxide layer on it's surface when exposed to air, this process is quite slow and subsequent preparation can remove the oxide in part. Another common material used in STM tip manufacture is platinum-iridium (Pt-Ir) alloy, it is a very unreactive metal which is formed in a different manner to tungsten. Both platinum and iridium are resistant to corrosion however, iridium alone is brittle and difficult to work, while platinum is relatively ductile and malleable. Iridium is added to the platinum to form an alloy, the result is a harder metal than native platinum and more easily manipulated than iridium. Other, more exotic material's have been used to produce STM tips, most notably carbon nanotubes have been used. They are dimensionally very appropriate, however, other physical parameters including their flexibility and piezoelectric properties makes them difficult to use and production is not as controllable as that of macroscopically produced metal tips.

High purity tungsten wire of diameter 0.25 to 0.3 mm is electrochemically etched to

form an apex tip, this tip can be dimensionally suitable for STM if etched in a controlled manner. The wire is partially submerged at one end into a bath of potassium hydroxide (KOH) or sodium hydroxide (NaOH) aqueous solution. The solution is approximately 8g solute (KOH/NaOH) to 50ml solvent (deionised water) or 16% by mass. The wire is submerged in such a way as to form a negative meniscus from the solution onto the wire, approximately 1mm of additional wire is then submerged, while maintaining the meniscus. An electrical current is passed between the wire that is not submerged and another electrode (typically stainless steel) within the bath. The resulting electrochemical process gradually etches the W wire in the form of the meniscus until the narrowing at the etched region causes the tip of the wire to break off into the solution. The remaining wire has an apex tip formed at the break point. The breaking of the wire causes a sudden drop in the current passing through the solution, this is used to detect the optimal time of formation and stop the etching process. This prevents the newly formed apex tip from being etched.

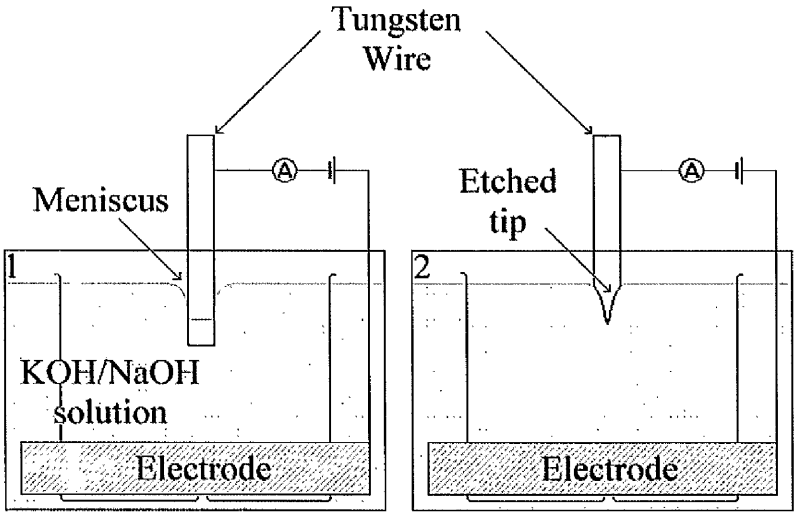

Figure 2.5.1-1: W tip etching process, 1) Before, and 2) After.

Within the tip etching apparatus used in this research the submerged electrode is circular and a partition composed of a second vessel concentric to the bath containing the solution is set up so that bubbles formed on it during the etching process do not disturb the surface of the solution near the tungsten wire. An aperture exists at the bottom of the partition to allow continuity of the solution. The whole unit is protected from vibrations by an anti-vibration system. The etching current usually starts at approximately 30mA and falls continuously over the etch process which takes approximately 15 minutes. Upon completion of etching the newly formed tip must be

removed from the solution and rinsed with deionised water, this ensures no contaminants remain to damage the tip. In particular crystals of KOH or NaOH which may form near the tip if residual solution is allowed to dry out. A native oxide will form on the surface protecting it from further corrosion, however, this oxide is undesirable for STM work as it may effect the tunnelling capability of the tip and produce a non-uniform DOS (Density Of States) profile for the tip. Subsequent tip cleaning can be performed using an accelerated beam of thermally ejected electrons. This process is performed in vacuum and will remove the oxide layer from the very end of the tip. In some situations it may be necessary to bring the tip back into atmospheric air in order to proceed with it's transfer into a usable position, in such circumstances the less time the tip is exposed to air the lower the probability of an oxide being re-formed upon it. If transferred within a minute or so back into vacuum the oxide may not return to a significant degree.

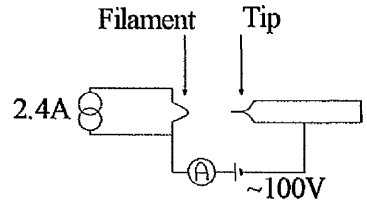

Figure 2.5.1-2: Tip e-beam treatment system.

The e-beam tip preparation method involves placing the tip coaxially opposite a heating filament. The filament is heated by passing a current through it to reach a suitable temperature so that electrons are thermally ejected from it. An electrical potential difference is set-up between the filament and tip (negative on the filament with respect to the tip) the resultant current produced by accelerating electrons across the vacuum gap (few millimetres) is used to bombard the very apex of the tip and dislodge or evaporate foreign material and the oxide layer. In this research the filament is held at a constant 2.4A and the filament-tip voltage is adjusted around -100V to maintain a filament to tip current of -0.1μA. This situation is maintained for approximately thirty seconds. A SEM (Scanning Electron Microscope) image of an STM tip before and after this treatment revealed significant improvement in the shape of the end of the tip. This is probably due to the ablation of foreign material from the tip. Hockett *et al.* used hydrofluoric acid to remove the native oxide from a tungsten tip and reported a noted improvement in tunnelling characteristics[17].

Pt-Ir tips are usually drawn as opposed to being etched. This relatively simple process involves cutting the Pt-Ir wire using a standard pair of wire cutters while at the same time drawing the wire laterally through the blades, the result is that very fine filaments of wire form and are drawn out at the very tip when the wire cuts through, it is also very likely that one of these filaments will be longer than the others and act as the dominant STM tip. This process is less controllable than etching for W tips but can produce some very sharp tips. Since this metal alloy is very stable it does not oxidise when exposed to air and since it has not been exposed to any other chemicals it is more likely to be clean at the tip. The subsequent e-beam tip treatment is usually not necessary for this material. Unused STM tips can be stored in air in a suitable holder and container to protect them from air currents and dust particles, however, for W tips it may be necessary to repeat the e-beam tip treatment before use. When stored in vacua this is not necessary.

2.5.2 AFM probe preparation

The AFM probe tips used in this research are silicon etched cantilever types. A chip of silicon is etched using standard lithographic techniques into a single crystal cantilever structure suitable for AFM. The tip is composed of three main regions: the chip body, which is used to mount the tip and support the cantilever; the cantilever arm, which allows elastic deformation of the crystal on a measurable scale and provides the opposing spring force in tip-surface interactions; and the tip itself which is a crystal structure at the end of the cantilever arm.

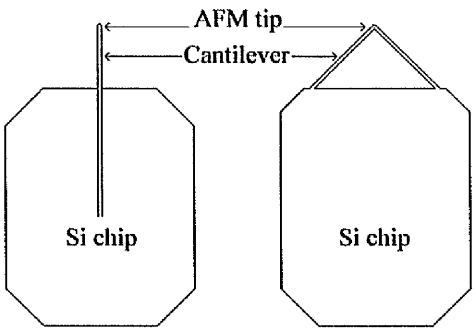

Figure 2.5.2-1: Two standard configurations of AFM probe.

Figure 2.5.2-1 shows two standard configurations of AFM tip the single and dual arm cantilevers. The probe on the left is a standard configuration that on the right is designed to be have a stiffer cantilever arm which resists lateral motion of the probe tip. The probe is mounted on a specially designed probe holder by gluing the chip body onto the

tip holder using a suitable glue. The glue must be rigid when cured, must not outgas when in vacua and where necessary facilitate electrical and thermal conduction. Vacuum compatible silver loaded epoxy resin glue is a suitable material for this purpose. The probe carrier has a hole behind the probe tip to allow the laser light to reach the back of the probe tip. It is not usually necessary to apply any further preparation of the tip before use, although careful rinsing with acetone may be used to remove any unwanted material from the probe.

In certain situations it may be necessary to modify the probe tip either by addition of other materials or further cleaning. The conducting AFM performed in this research used AFM probes coated in a thin metal film including gold and Pt(80%)-Ir(20%) alloy. Prior to coating the probe was dipped into a bath of acetone to remove unwanted material. The probe was then mounted in an evaporation plant chamber. At an ambient pressure of 10^{-5} torr. High purity metal wire was evaporated by heating in a tungsten wire crucible. The resultant free metal atoms are released in all directions and form a thin film on whatever surface they land, including the AFM probe situated approximately 15cm away for gold evaporation and approximately 5cm away for Pt-Ir coating.

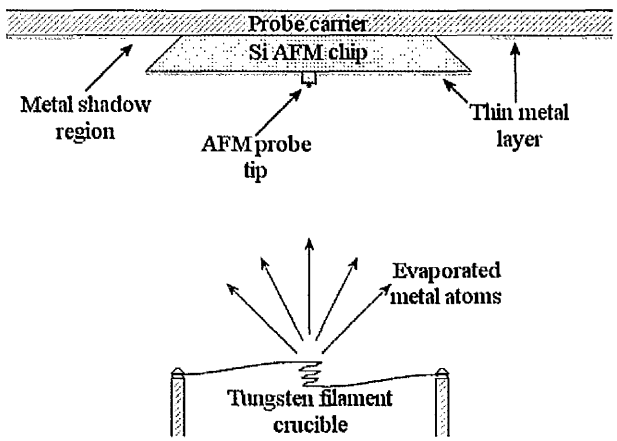

Figure 2.5.2-2: AFM probe metal coating.

The metal atoms coat the AFM probe and the probe carrier except in a region directly beneath the silicon probe chip edges. The overhanging edges are a result of the natural cleavage planes of silicon. This shadow region must be bridged by a conductor. Silver loaded epoxy is a suitable choice for this.

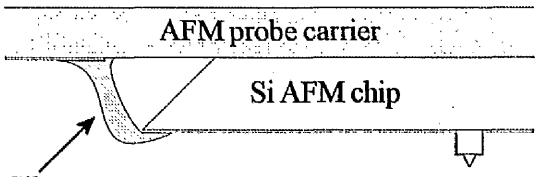

Figure 2.5.2-3: Conducting bridge over metal shadow region of coated AFM probe.

This additional conducting path ensures complete low impedance ohmic conduction from the probe carrier back contact and the AFM probe tip.

2.5.3 Sample Preparation

Sample preparation is a very critical part of SPM and varies considerably depending on the sample being investigated and the technique being used. Robust samples such as the nitrides grown on sapphire can be subjected to handling that would destroy other sample materials such as GaAs based materials or nano-particle structures deposited on another substrate such as silicon. Likewise chemical cleaning and preparation suitable for use with one material may result in damage or the complete annulment of another material specimen. Some materials investigated in this research can react with their environment (atmospheric gasses) over time rendering previously performed preparation void. Cleaving also is a material specific process requiring knowledge of the crystal structure of the sample being cleaved and the orientation of the crystal planes relative to the sample being cleaved.

2.5.3.1 Cleaning

Cleaning samples involves removing any foreign material that may exist on the material or occasionally removing an oxide layer coating it. Contaminants usually include dust and fine particles, grease, oil, and other hydrocarbons, and water. Solvents are commonly used to remove these materials. With most materials including GaAs GaN and Si water may be used to remove dust and some particles. Water itself is, however, usually not a desirable component when investigating material properties. Dust and other small particles may be removed using alcohols such as isopropyl alcohol and methyl alcohol or the ketone, acetone, these chemicals tend to evaporate, leaving a dry material surface void of moisture, however, if particles are left on the material's surface during drying the particles can be swept up by the surface tension of the receding liquid forming a cluster at the last point of evaporation. It is, therefore, more usual to ensure

the removal of foreign particles beforehand. Soft tissues or cotton wool may be used to agitate foreign materials in conjunction with the use of a solvent such as water or acetone. Grease and oil are complex hydrocarbons which are most effectively removed by dissolving them with a degreasing solvent. Acetone is commonly used for light contamination and can dissolve a wide range of hydrocarbons, however, with more complex hydrocarbons including wax trichloroethylene (trike) is the preferred solvent. This solvent should in turn be dissolved in methanol to remove. Pressurised nitrogen gas can be used to remove dust by blasting it off the surface and to increase the rate of evaporation of solvents. This last procedure is useful since solvents have a tendency to collect particles and dust from atmospheric sources. Certain materials such as a nano-particle system deposited on substrate such as silicon may have low surface adhesion and could be damaged by the procedures indicated above, in general such materials require careful handling to reduce their exposure to contaminants. The native oxide that forms on silicon can be removed by controlled rinsing in hydrofluoric acid.

2.5.3.2 Cleaving and edge preparation

Cross sectional probe microscopy requires the exposure of a cross section of the materials being investigated. Various techniques exist to produce a suitable cross section. Standard cleaving techniques were used to access material edges along with novel breaking and bevelling techniques.

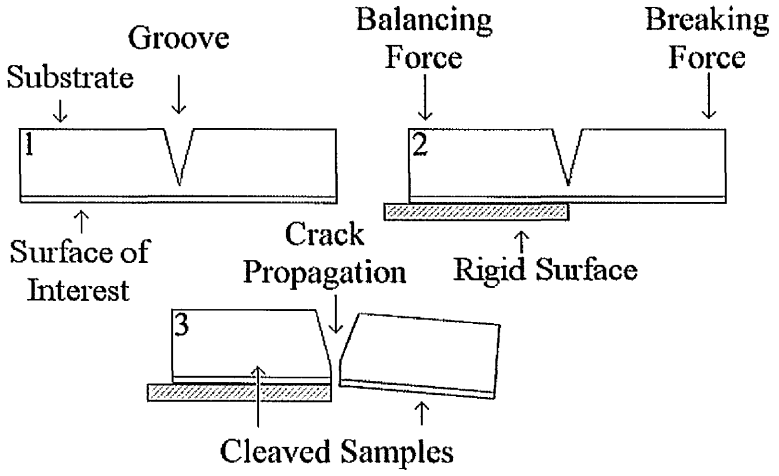

Figure 2.5.3.2-1: A typical three stage cleaving process.

Figure 2.5.3.2-1 shows a typical three stage cleaving process. The desired crystal plane is located and a groove parallel to the crystal plane or a notch is created in the substrate of the material. Forces are applied which then cause a crack to form and propagate through the material to the other side. The groove provided a weak point which instigates and guides the cleave. In this research the last two stages were usually performed in vacuum for direct transfer into the STM or AFM, this ensures a clean contamination free surface. Some materials cleave on known cleavage planes easier than others, with such materials it is often less advantageous to mark a groove in the sample's substrate than it is to place a small indentation in the substrate to act as a weak point in the formation of cracks. A micro indentation system was used in which a weighted diamond tip is impressed into the material's substrate in a controlled manner. The result is an indentation which in GaAs based materials will readily be the source of crack propagation along the desired crystal plane. Sample thinning was also used to reduce the force required to cleave the material. The samples substrate is ground using an abrasive such as Al_2O_3 in particle or resin held particle form. A sample with a 300μm thick substrate can be reduced to 100μm thick without compromising the material to be investigated.

These standard techniques were found to be ineffective with GaN on sapphire materials, the substrate did not follow prescribed markings and broke in unpredictable directions. A new process was performed to produce a guided material break with the intention of approximating a cleavage plane. Since a crystalline material will break along cleavage planes and involve steps in the plane to accommodate breaking in a direction close to a cleavage plane a guided break may present regions of investigable material.

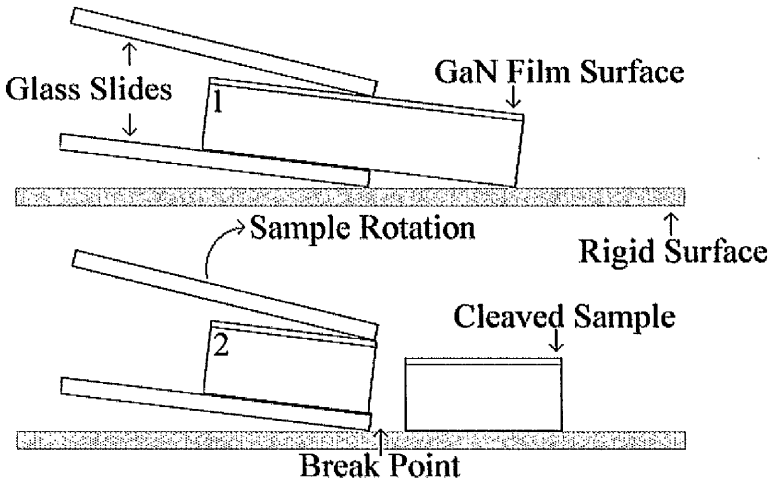

Figure 2.5.3.2-2: A guided breaking process for use with sapphire.

Figure 2.5.3.2-2 shows the two stage process for controlled breaking of sapphire, the sample material is sandwiched between two glass slides, the upper of which has a slight incline to the plane of the sample and is convergent with it at the desired breaking point which is parallel to the lower glass slide. The two slides and hence the sample is rotated as depicted in the figure, the resultant tensile stress produced on the substrates surface causes a crack to propagate through to the material's surface at the point at which the upper glass slide meets the surface. This method produces visually flat breaks and under a standard microscope the material appears flat. Although the translucent nature of the material reduces effective regional contrast.

Sample bevelling as a method to prepare a surface for SPM investigations is a novel technique. The concept arose as a need to access the sub surface layers for investigation became necessary. By bevelling the material sample the epitaxial layers can be revealed by lateral scanning from the top surface of the material.

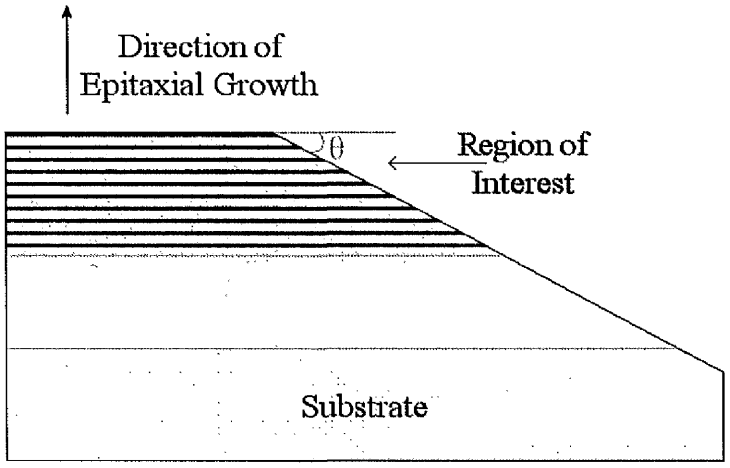

Figure 2.5.3.2-3: A bevelled sample revealing features in the epitaxial direction.

The sample is bevelled by mounting the substrate onto an angled surface and grinding down the exposed portion using a suitable abrasive such as diamond paste (particles of diamond in a lubricant suspension). Subsequent cleaning and chemical etching are necessary to produce a smooth surface.

Molten potassium hydroxide and a high temperature potassium hydroxide or sodium hydroxide solution in ethylene glycol are able to chemically etch gallium nitride[18].

It may be necessary to coat the sample material in a metal film to provide an ohmic contact. A clean sample can be placed into an evaporation coating plant and the metal heated to the point of evaporation in a similar manner to that used to coat the AFM probes in a metal conducting layer. The metal will form a thin film on the surface of the material exposed to the beam of metal atoms. The area of exposure can be augmented by apertures to produce contact spots.

The shallow gradients used in bevelling such as 1:50 would not present a problem to an STM, the feedback loop can easily compensate for this gradient and the slope could be removed from the data using the methods described earlier.

2.6 References

1. G. Schott *Mechanica hydraulico-pneumatica* **1657**.
2. I. Giaever *Phys. Rev. Lett.* **1960**, *5*, 147.
3. L. Esaki *Phys. Rev.* **1957**, *109*, 603.
4. G. Binnig, H. Rohrer, CH. Gerber, and E. Weibel, *Appl. Phys. Lett.* **1981**, *40*, 178.
5. G. Binnig, H. Rohrer, CH. Gerber, and E. Weibel, *Phys. Rev. Lett.* **1982**, *49*, 57.
6. J Tersoff, DR Hamann, *Phys. Rev. Lett.* **1983**, *50*, 1998.
7. J Tersoff, DR Hamann, *Phys. Rev. B*, **1985**, *31*, 805.
8. TE Feuchtwang, PH Cutler, NM Miskovsky, *Phys. Lett.* **1983**, *99A*, 167.
9. ND Lang, *Phys. Rev. Lett.* **1986**, *56*, 1164.
10. J Bono, RH Good, Jr. *Surf. Sci.* **1985**, *151*, 543.
11. J Bono, RH Good, Jr. *Surf. Sci.* **1986**, *175*, 415.
12. RM Feenstra, JA Stroscio, J Tersoff, AP Fein, *Phys. Rev. Lett.* **1987**, *58*, 1192.
13. GFA van de Walle, H van Kempen, P Wyder, *Appl. Phys. Lett.* **1987**, *50*, 22.
14. NM Amer, A Skumanich, D Ripple, *Appl. Phys. Lett.* **1986**, *49*, 137.
15. S Grafström, J Kowalski, R Neumann, O Probst, M Wörtge, *J. Vac. Sci. Technol. B*, **1991**, *9*, 568.
16. G Binnig, CF Quate, Ch Gerber, *Phys. Rev. Lett.* **1986**, *56*, 930.
17. LA Hokett, SE Creager, *Rev. Sci. Inst.* 1993, *64*, 263.
18. DA Stocker, EF Schubert, JM Redwing, *Appl. Phys.Lett.* **1998**, 73, 2654.

Chapter 3: STM investigation of a novel mixed Type I – Type II GaAs/AlAs structure.

3.1 Introduction.

Novel photosensitive structures are of great interest to condensed matter physics. The potential for device application and furthering the understanding of physical processes makes such materials an important focus for condensed matter research.

The group III-V compounds such as GaAs and GaN are commonly used materials for optical devices in the near infra-red to near-ultraviolet region of the electromagnetic spectrum. GaAs based devices are typically used in the near infra-red to red light region, the latter usually when combined with another material such as Al often in a ternary compound $Al_xGa_{1-x}As$. While a p-n junction is usually required for electroluminescence as used in Light Emitting Diodes (LEDs), optically active semiconductor devices do not necessarily require them. This research concerns a novel mixed type I – type II structure composed of a stack of 20 periods of an alternating width double quantum well system. The quantum wells are GaAs and the barriers are AlAs. The wider of the two wells is 68Å thick and the narrower of the two wells is 25Å thick while the barrier is 93Å thick. This arrangement allows for some of the properties unique to this material system. A profile of the complete structure is presented in figure 3.1-1. A single period of the 20 period stack in the complete structure (to the right of figure 3.1-1) is shown on the left of figure 3.1-1. The 20 period structure is the active region of this material. This material is novel because of the unique combination of type I and type II band alignments. The type II alignment originates in the narrow GaAs quantum well, wherein the lowest electron state is at Γ and is greater in energy than the X minimum in the AlAs barrier. The type I band alignment originates in the wide GaAs quantum well, in this case the Γ minimum in the well is lower in energy than the X minimum in the AlAs barrier. The Γ point is a direct bandgap point. The X point is an indirect bandgap point.

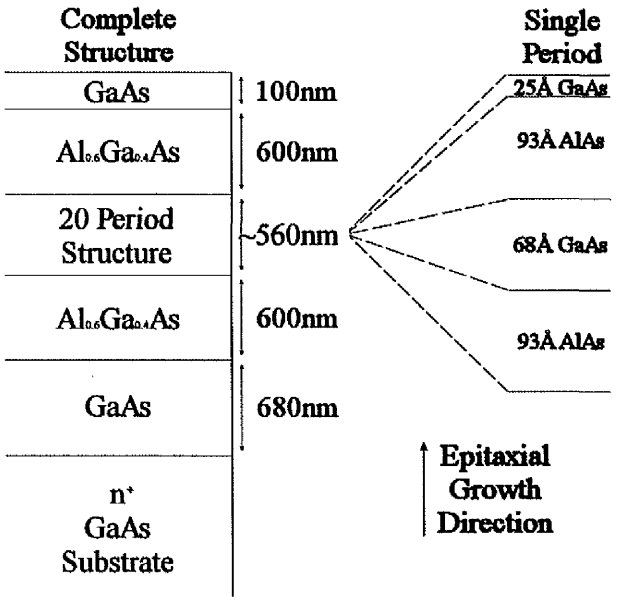

Figure 3.1-1: Complete structure profile, not to scale.

The mixed type I – type II material structure was produced by the epitaxial growth technique, Molecular Beam Epitaxy (MBE). The MBE epitaxial growth system allows growth of epitaxial structures one monolayer at a time, this results in a high degree of control over the material's composition.

3.1.2 Material Properties

Figure 3.1.2-1 shows the photoelectric interactions of the mixed type I – type II material. When the direct bandgap in the narrow quantum well (type II alignment) is pumped optically at a suitable wavelength λ_1 (greater than the lowest transition energy) an electron-hole pair are produced (1). The electron then scatters from the Γ state to the X state in the AlAs barrier on a sub-picosecond time-scale[1](2). The electron is then scattered from the X state to the Γ state in the wide quantum well (type I alignment) over a time-scale of approximately 30 picoseconds, this increased scattering time is due to the low density of Γ states in the wide quantum well[1] (3). There is no fast scattering path for the hole to follow and so the electron and hole are separated until the electron or hole is thermally exited back to the other or the hole tunnels through the barrier to the wide well (4) whereupon the electron and hole recombine and emit a photon of energy equal to the energy gap of the wide quantum well λ_2 (5). It is worth noting that the wide quantum well is also excited by the light source used to excite the narrow quantum well.

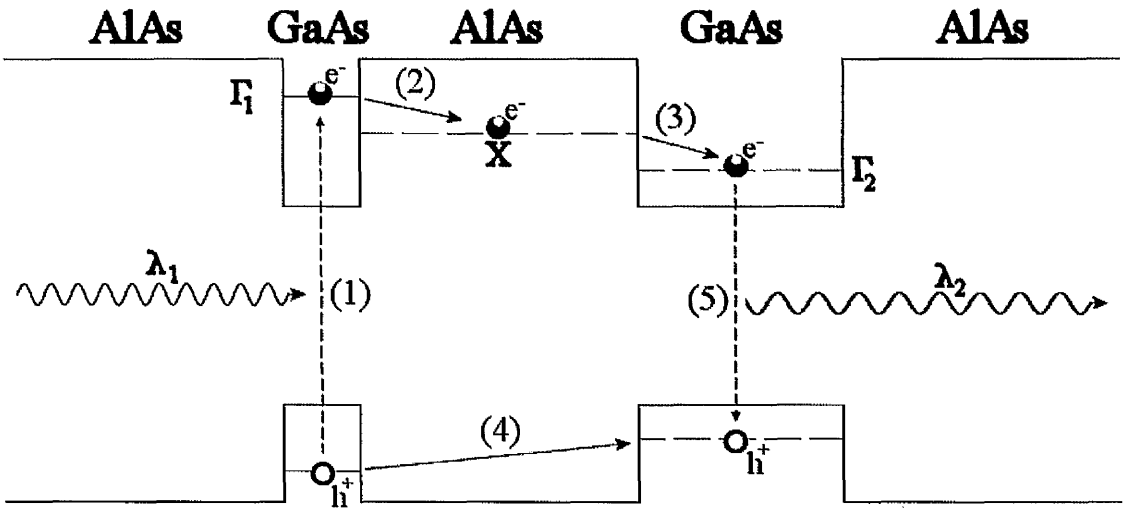

Figure 3.1.2-1: Photoelectric interactions of mixed Type I - Type II material.

At room temperature the electrons and holes are thermally distributed between the wells following a Boltzmann distribution. At the liquid nitrogen temperatures (~77K) the thermal tail from the Boltzmann distribution reduces so that thermal excitation of electrons and holes becomes insignificant and due to the long tunnelling time of the order of microseconds for the hole from the narrow well to the wide well[1-2], therefore, spatially separated electron and hole plasmas are produced in the wide and narrow wells respectively. A 2-DEG (2-Dimensional Electron Gas) forms in the wide well and a similar hole gas forms in the narrow well. Remarkably little illumination is required to produce these electronic phenomenon[1-3].

A computer program[4] was used to calculate the allowed electron and hole energy levels in individual wide and narrow quantum wells equivalent to the wide and narrow quantum wells in this material's structure. Some material characteristics can be predicted from these data. For the narrow well the pump laser light source λ_1 (632.8nm, 1.96eV) is able to create an exciton from both of the ground state e-hh and e-lh transitions in the narrow well, the ground state e-hh , e-lh and the second state e-hh and e-lh transitions in the wide well. Table 3.1-1 shows a complete list of allowed electron-hole transition energies. The lowest energy of recombination from the ground state in the wide well at a temperature of 77K is 1.59eV which corresponds to a light emission wavelength λ_2 of 799.9nm. Although GaAs has a bandgap of 1.42eV at 300K this increases to 1.51eV at 77K.

Well	*n*	*Transition*	*Energy (eV)*
Narrow	1	e-hh	1.808466
Narrow	1	e-lh	1.894322
Wide	1	e-hh	1.591708
Wide	1	e-lh	1.622501
Wide	2	e-hh	1.812429
Wide	2	e-lh	1.921102
Wide	3	e-hh	2.059421
Wide	3	e-lh	2.243013

Table 3.1-1: Narrow and Wide well transition energies at 77K.

This material has been used as an attenuator of terahertz radiation[5]. By optically exciting the mixed type I – type II material to change the normally semiconducting wide wells into a metallic 2-DEG, modulation of a terahertz beam can be realised[5].

3.2 Objective

The objective of the research into this material is to characterise the material's structure and compare with the growth parameters, to image the electron and hole gasses and to investigate the relationship between the illumination and the electronic behaviour, specifically including the tunnelling current at various locations across the material's structure. This should reveal the transition from the thermal distribution of carriers in the wells with little or no light to the distinctly separate electron and hole plasmas.

The material was grown using the very controllable MBE process and so should be accurate to within one or two atomic layers as far as each part of the structure extends. There will be localised fluctuations of the well/barrier width within a single well/barrier due to the nature of the growth process, however, these should average out over an entire well/barrier.

3.3 Method

In order to characterise the 20-period active region of the material's structure the material was cleaved in UHV to present a flat and clean cross sectional surface on which to perform X-STM. The STM tip was located over the cleaved edge in the vicinity of the 20 period structure in a similar manner to that depicted in figure 2.3.2.5-1. The STM was scanned over the structure and surrounding layers with and without illumination from an incandescent light source and with and without illumination from a 15mW He-Ne laser; at both room and liquid nitrogen temperatures. By varying the applied tip-sample electric field (gap voltage) it becomes possible to "tune-in" to different electronic features. This method was used to produce high contrast images of the active region of the structure and to reveal spatial electronic information apart from topographical information.

Once imaged at low temperature a number of *I/V* spectra were taken at a range of laser light intensities, from full power to no external light source. A set of eight equal neutral density filters with equal transmission coefficients at 632.8nm wavelength light of 20% were used to attenuate the laser light. This should reveal the formation of the electron and hole plasmas.

Another technique used is the lock-in technique. The laser light was passed through a mechanical chopper to produce a pulse train of light incident upon the sample's surface. The component of the current measured by the STM tip that was related directly to the pulsed light source was then locked-into by the lock-in amplifier. This process eliminates virtually all components of the current signal which are not directly related to the photoelectric characteristics of the material. The resulting signal was recorded along side the standard current *I* and *Z* signals. The pulse frequency was set so as not to induce oscillations in the *Z* signal. This arrangement is as described in chapter 2.3.2.6 and depicted in figure 2.3.2.6-1.

With the exception of figure 3.4-1 all of the presented data was taken at liquid nitrogen temperature (77K).

3.4 Results and Discussion

Early imaging of the quantum well structure revealed a 20-period structure surrounded by layers of similar size to those described in figure 3.1-1. Imaging was produced at room temperature and with illumination from an incandescent (halogen) lamp with a dichroic filter to reflect heat backwards, away from the sample.

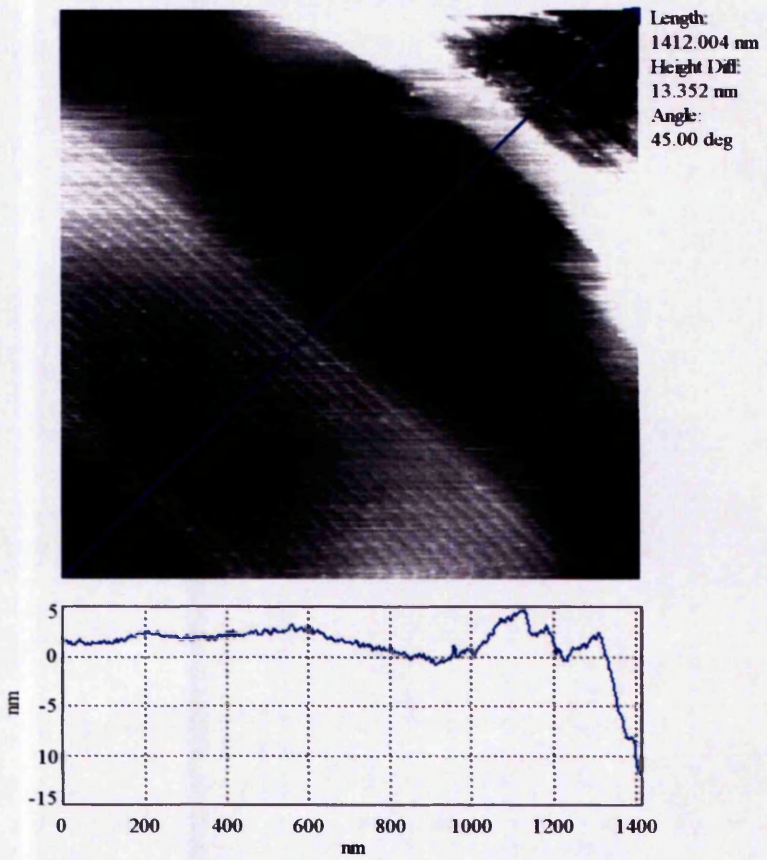

Figure 3.4-1: 1 x 1 μm image of MQW structure including all subsequent layers to surface.

Figure 3.4-1 shows a 1 micron square image of the structure of the mixed type I – type II material. The image was taken at an angle of 45 degrees to the epitaxial growth direction. The image includes all of the layers grown on top of the Multiple Quantum Well (MQW) structure. A line profile demonstrates the difference between the magnitude of electronic information (the wells) in comparison to topographical information (the rough material towards the edge). The STM tip tracks off the surface edge of the material in the top right corner of the image. An electrical potential difference of -6.0V was applied to the sample with respect to the tip. The tunnelling

current was 0.24nA. It should be noted that there only appears to be one set of bright and dark features in this image, 20 periods. Only one set of the wells are being imaged.

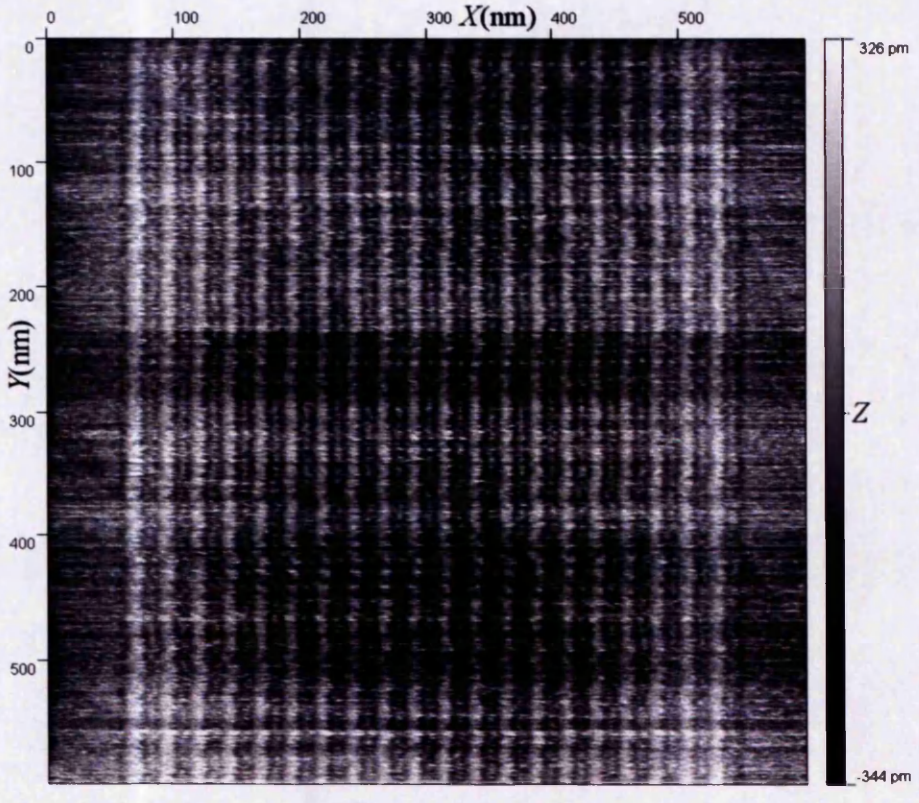

Figure 3.4-2: High resolution image of the full 20 period MWQ structure.

Figure 3.4-2 is a tip-height (Z) image, which shows the full 20 period MQW structure, with this resolution it is possible to image the other well as a darker line between the bright lines. From the structure parameters it can be inferred that the darkest lines are the barriers. The bias voltage was -7.22V on the STM sample and the current set-point was 1.0nA. Image taken with incandescent light. Figure 3.4-2 was taken at liquid nitrogen temperature (77K).

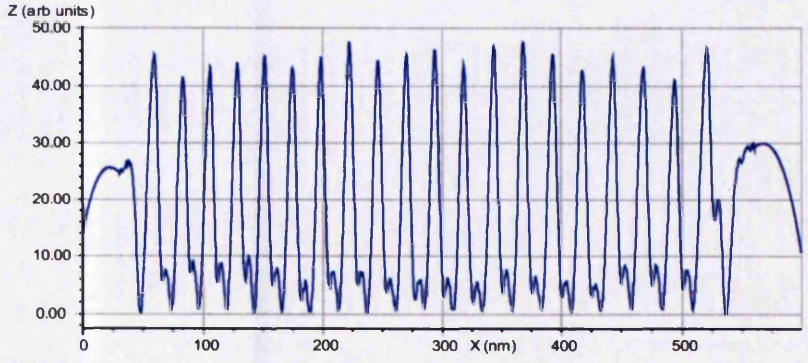

Figure 3.4-3: An averaged line-scan through figure 3.4-2.

Figure 3.4-3 shows the set of wells in between the prominent set. The roll-off at both ends of the image is due to a post processing method used to correct for a background surface slope. There is some evidence of a double peak within the less prominent well set. From the growth parameters the order of the wells can be determined. The more prominent wells in figures 3.4-2 and 3.4-3 are the wide wells and the less prominent wells are the narrow wells. From left to right after the initial barrier is a wide well, then a barrier, then a narrow well. The set is terminated with a narrow well and a final barrier.

Imaging was optimised by improving tip production to increase sharpness and by reducing cleaving to imaging times to reduce sample contamination. This greater resolution enabled the complete resolution of both the narrow and the wide quantum wells.

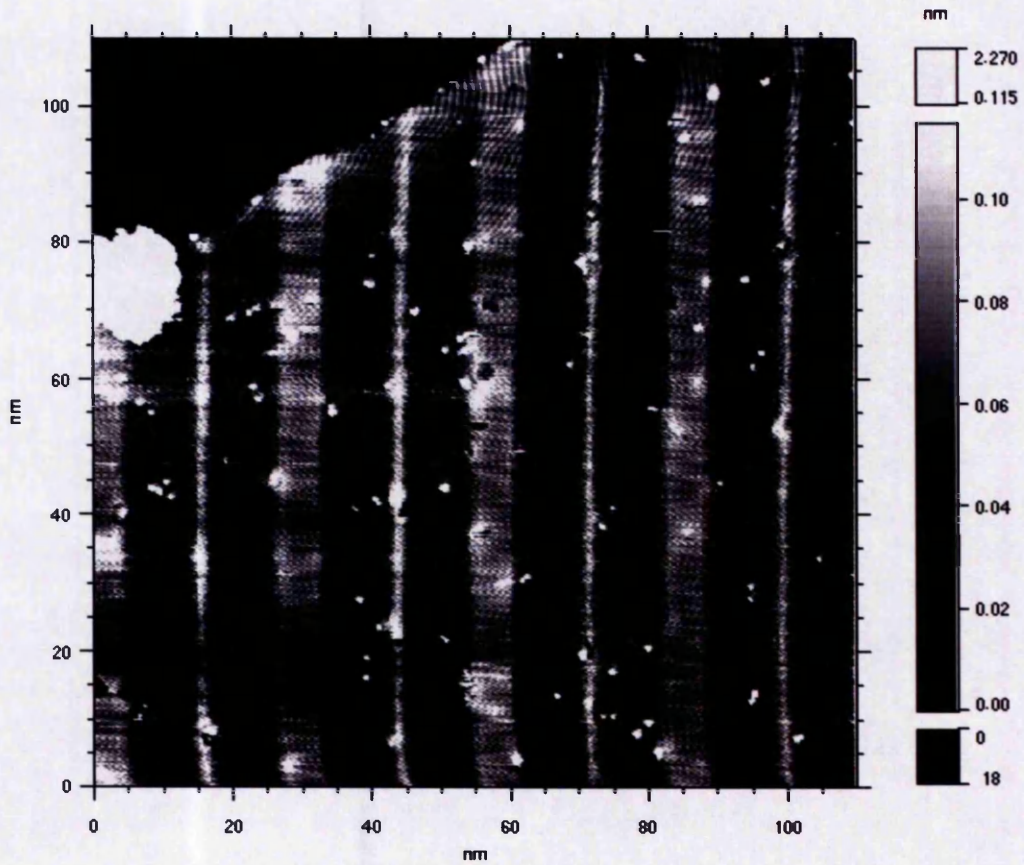

Figure 3.4-4: Very high resolution imaging of electronic structure.

Figure 3.4-4 shows high resolution imaging of both the narrow and wide quantum wells. The wells are clearly resolved enough for characterisation. The light and dark blobs on the image of the sample's surface are adsorbed material. Over time this increases in quantity and tends to cluster, eventually reducing maximum achievable resolution. The region to the top left of the image is an inward step in the surface topography, with the *Z* resolution used for imaging the electronic structure the topographical features are very prominent and can obscure the electronic information in some cases. This is in stark contrast to figure 3.4-2, where topographical steps are visible beneath the electronic structure imaging (running diagonally from top-left to bottom-right). The applied gap-bias was -7.2V on the tip and the current set point was 0.24nA. Temperature was 77K. The polarity is opposite for this image. The sample was illuminated by both 15mW He-Ne gas laser at a wavelength of 632.8nm and incandescent light. Vibrations from an unknown source in the building are also visible as a wavy Moire-like pattern, these are

particularly noticeable toward the top of the image.

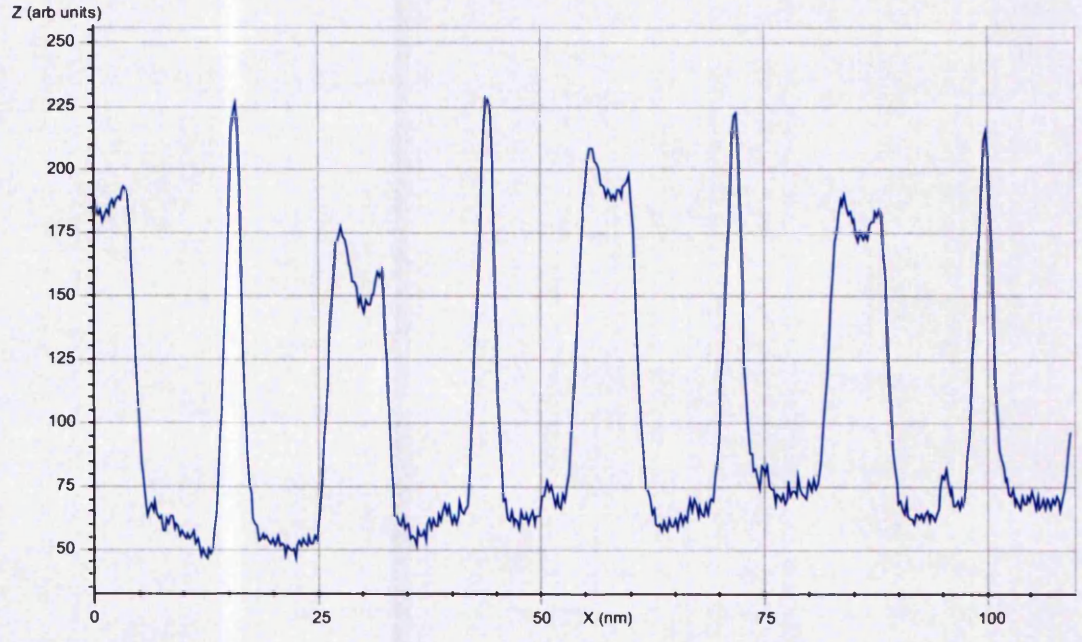

Figure 3.4-5: An averaged linescan through figure 3.4-4 showing wide and narrow wells.

The line-scan in figure 3.4-5 shows the electronic features from image 3.4-4, the narrow and wide wells are clearly distinguishable. The appearance of the double peak in the wide wells is interesting and comparable to the possible double peak in the less prominent (narrow) wells in figures 3.4-2 and 3.4-3.

From the three fully visible wide wells the average width is measured as 6.78±0.01nm, for the narrow wells are 2.73±0.01nm and the barriers are 9.31±0.01nm. This does not account for any error in the STM's positional calibration or broadening from the STM tip, however, it is very similar to the material specifications.

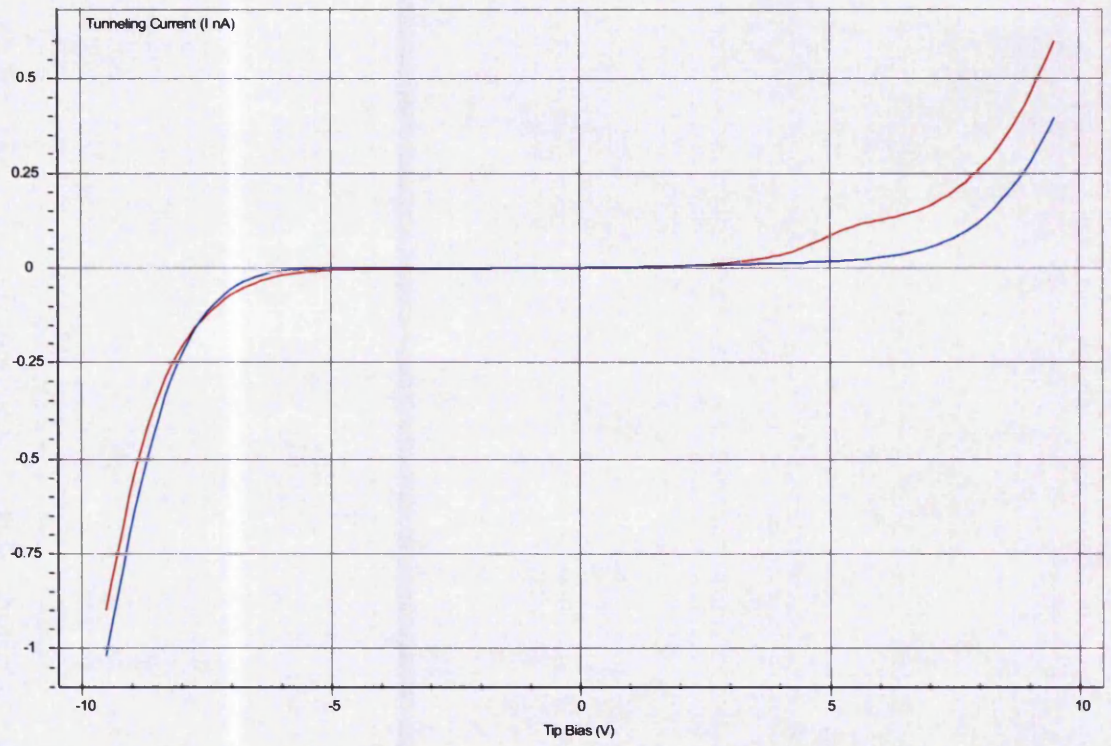

Figure 3.4-6: Spectroscopy of wide(Red) and narrow(Blue) quantum wells, illuminated by He-Ne laser.

Figure 3.4-6 shows *I/V* spectroscopy taken on the wide (red) and narrow (blue) wells. The region near +6V tip bias shows the increased electron gas in the wide well under illumination. This corresponds to the increased magnitude (*Z*) of the wide wells in figures 3.4-2 and 3.4-3. Figures 3.4-4 and 3.4-5 correspond to the region near -7V tip bias. In this region the magnitudes (*Z*) of the wide and narrow wells are similar but in this regime that of the narrow well is slightly larger than the wide well, a crossover point is noticeable in the *I/V* data near -8V tip bias.

Figure 3.4-7 shows a log-plot of *dI/dV* which can be used as a measure of the density of states. The two dimensional electron gas in the wide wells (red line) is again visible at +5V tip bias and the log plot reveals a complimentary depression in the narrow wells (blue line).

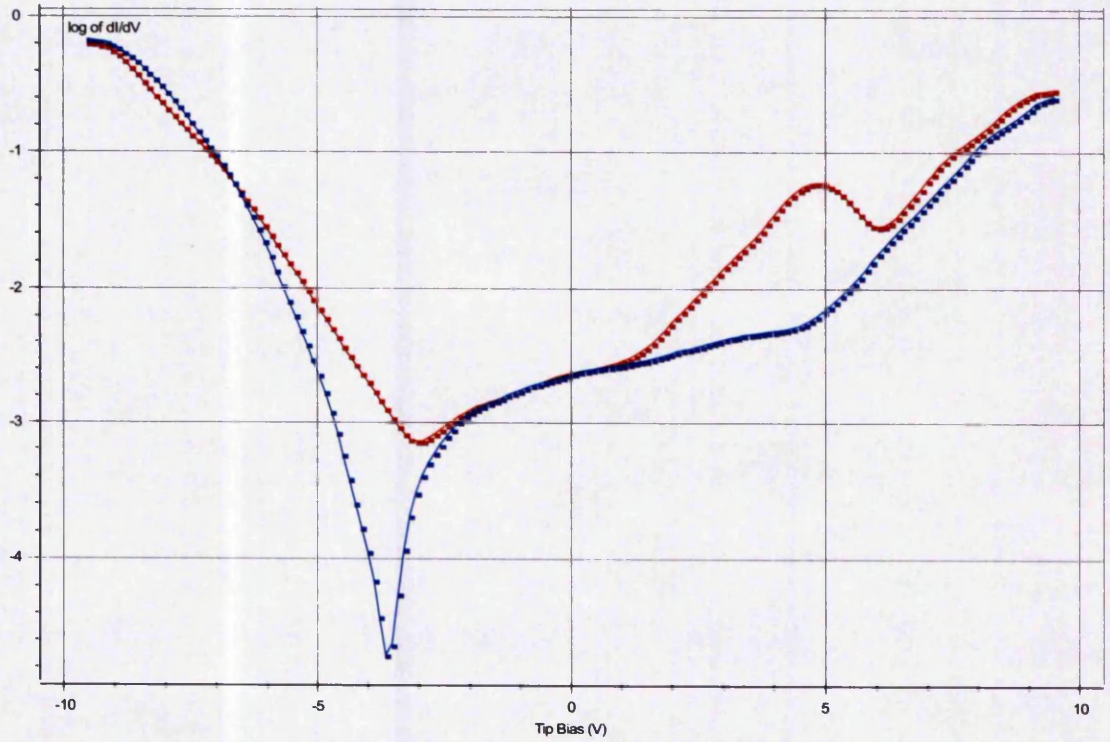

Figure 3.4-7: Log plot of dI/dV for wide (Red) and narrow (Blue) quantum wells.

The normalised differential conductivity plot can be obtained by dividing *dI/dV* by *I/V*, this plot is actually the ratio of the differential conductivity to total conductivity.

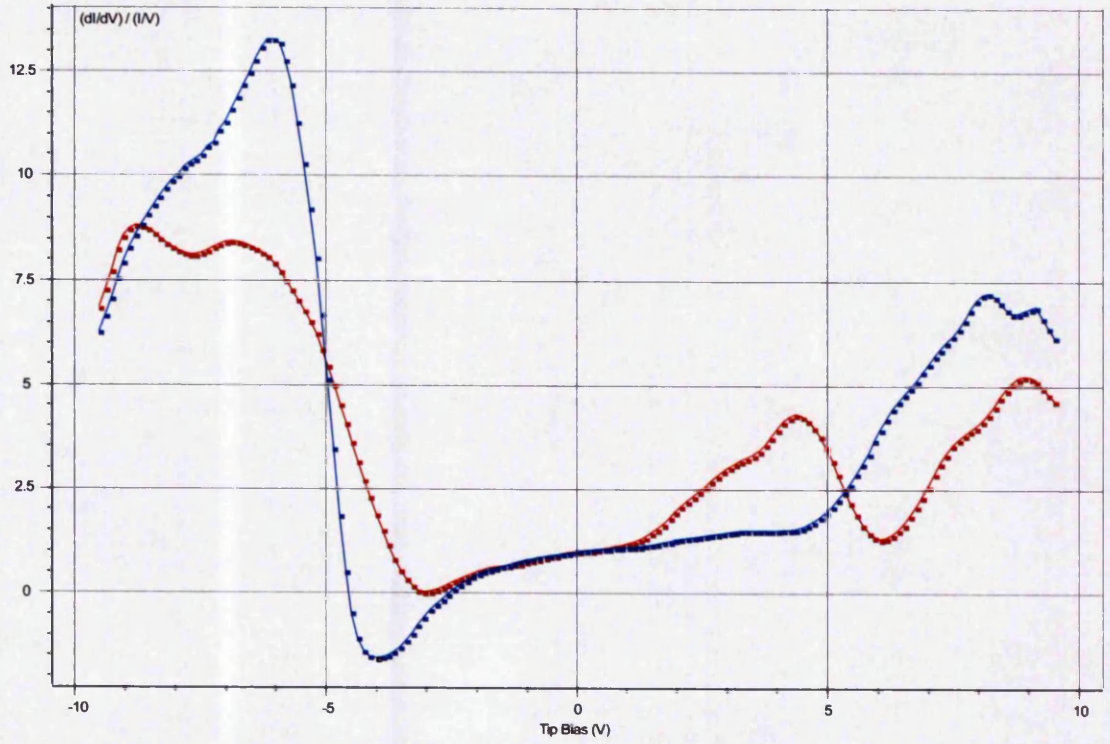

Figure 3.4-8: Normalised differential conductivity for wide (Red) and narrow (Blue) quantum wells.

The process of calculating the normalised differential conductivity removes most of the dependence of the differential conductivity on tip-sample separation and applied tunnelling bias[6]. The result is a more accurate representation of the density of states at an applied bias than a raw *dI/dV* and it is not necessary to stretch the data out in a log plot to visualise the full dynamic range.

An attempt was made to map the relationship between the *I/V* spectra and the illumination intensity. A 15mW He-Ne laser beam at 632.8nm was targeted at the tip-sample interface without any focussing to ensure a good overlap with the tunnelling junction. The beam passes through any external filters present, one plane of glass and two planes of quartz before reaching the sample. The beam is not focussed and the full intensity incident at the sample's surface is referred to as W_0.

An estimate based upon Snell's law[7],

$$n_1 \sin\theta_1 = n_2 \sin\theta_2 \qquad 3.1$$

for an incident ray in media with refractive index n_1 and angle of incidence relative to normal of θ_1 entering a second transparent media with refractive index n_2 the angle of emergence within the second medium is θ_2 relative to the normal,

and Fresnel's equations,

$$t_{\parallel} = \frac{2\sin\theta_2\cos\theta_1}{\sin(\theta_1+\theta_2)\cos(\theta_1-\theta_2)} \qquad t_{\perp} = \frac{2\sin\theta_2\cos\theta_1}{\sin(\theta_1+\theta_2)} \qquad 3.2$$

where t is the transmission coefficient for parallel and perpendicular polarisations of light, suggests that ~77±10% of incident light at the windows of the vacuum chamber will fall upon the tip-sample interface. So incident power is approximately 11.5mW. Assuming an even non diverging beam with a diameter of 1mm the intensity would be approximately $W_0 = 1\text{Wcm}^{-2}$.

At low optical intensity and low temperatures the tunnelling current reduces causing the tip to crash into the surface of the material. It is not possible to maintain positional accuracy on the material's surface without a tunnelling current. van de Walle *et al.* experienced a similar problem while performing STM on GaAs and used a light source to promote carriers to enable conductivity[8].

The lock-in amplifier technique as described in chapter 2.3.2.6 was used to extract only the current data pertaining to the optical excitation of the sample. This method would demonstrate the spatial dependence of the tunnelling current on light without

compromising the STM tip. The laser was modulated at a frequency of 230Hz using a mechanical beam chopper and used as a reference for a Stanford Research Systems SR830 lock in amplifier. The output from the lock in amplifier was recorded simultaneously with the *Z* data from the feedback loop of the STM. The rapidly pulsing beam allowed the feedback loop to partially decouple from the light intensity changes and maintain a constant *Z* position during the rapid changes in light intensity. The result is that the electronic information specific to light intensity can be recorded without crashing the STM tip into the sample's surface.

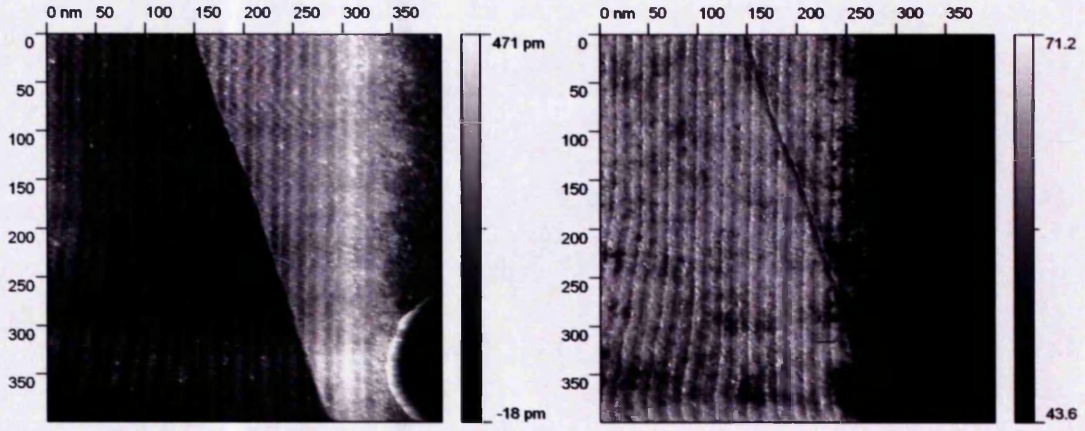

Figure 3.4-9: STM Z image and LIA image of same region.

Figure 3.4-9 shows a standard *Z* image (left) and the equivalent LIA image (right). The topographic step shown as a diagonal line and change in image brightness in the *Z* image is only shown as a transient mark in the LIA image. To the right of the images the quantum well stack finishes and leads in to the next material $Al_{0.6}Ga_{0.4}As$. This is visible in the LIA image as a dark region where very little response to the light is occurring. Interestingly the response of the current to the light appears to drop off before the actual material change, this happens over the last three periods of the structure, a region of approximately 100nm. The last wide and narrow wells also appear to be more prominent than their neighbours in the *Z* image. The *Z* image was taken at -7V and with a tunnelling current set point of 0.22nA.

3.4.1 Analysis

A numerical calculation[4] for an isolated wide and an isolated narrow well equivalent to those in this material shows a set of electron and hole wavefunctions at eigenstates within the quantum wells. The bandgap of the well at 77.0K is 1.5076eV.

Well (Å)	Eigenstate	Energy from Band Edge (eV)
Narrow (25)	E1	0.227063
Narrow (25)	E2	0.414213
Narrow (25)	HH1	-0.073808
Narrow (25)	HH2	-0.283292
Narrow (25)	LH1	0.159664
Wide (68)	E1	0.067577
Wide (68)	E2	0.239237
Wide (68)	E3	0.406738
Wide (68)	HH1	-0.016536
Wide (68)	HH2	-0.065597
Wide (68)	HH3	-0.145087
Wide (68)	HH4	-0.250217
Wide (68)	HH5	-0.371502
Wide (68)	LH1	-0.047329
Wide (68)	LH2	-0.174270
Wide (68)	LH3	-0.328679

Table 3.4-1: List of eigenstates in the narrow and wide wells at 77K.

Table 3.4-1 presents the calculated electron and hole eigenstates within the narrow and wide quantum wells, note E denotes an electron eigenstate, HH denotes a heavy hole eigenstate and LH denotes a light hole eigenstate. All energies are quoted with respect to their respective band edge. A numerical solution[9] to the Schrödinger-Poisson equation based upon a single dimensional 25Å and 68Å wells composed of GaAs sandwiched between two layers of AlAs barriers also shows the wavefunctions of the electron and hole states within the quantum wells. These finite quantum well models are used to provide a baseline for the eigenstates and their wavefunctions. The wavefunctions tail off and become insignificant very quickly outside of the wells, this allows for the excellent electron-hole spatial confinement within this material and hence the long recombination lifetimes dominated by the slow hole tunnelling process. From

the calculated wavefunctions the first heavy hole HH1 wavefunction value has fallen to one millionth of its peak value just 50Å from the edge of the wide well.

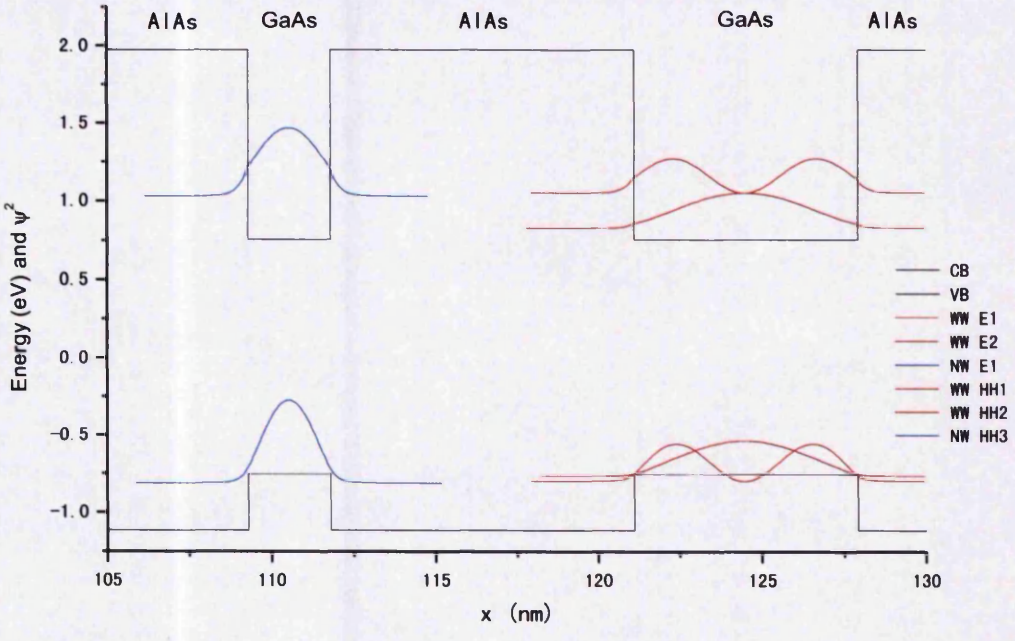

Figure 3.4.1-1: Electron and hole wavefunction probabilities for the narrow and wide quantum wells.

Figure 3.4.1-1 Shows the electron and hole eigenstates for the narrow and wide quantum wells, the electron and hole wavefunction probabilities are overlaid with the baseline eigenstate energy to assist in visualisation. Of course the depicted probability distribution for each eigenstate is the square of that eigenstate's wavefunction.

Well (Å)	Eigenstate	Energy from Band Edge (eV)	
		Numerical Solution	Schrödinger-Poisson
Narrow (25)	E1	0.227063	0.274980
Narrow (25)	HH1	-0.073808	-0.058050
Wide (68)	E1	0.067577	0.074750
Wide (68)	E2	0.239237	0.299300
Wide (68)	HH1	-0.016536	-0.010275
Wide (68)	HH2	-0.065597	-0.043352
Wide (68)	HH3	-0.145087	-0.102403
	Bandgap	1.507596	1.50793

Table 3.4-2: Comparison of numerical solution and Schrödinger-Poisson solution for quantum well values at 77K.

Table 3.4-2 compares the eigenstate energies calculated in the numerical solution presented in table 3.4-1 and the results produced by the Schrödinger-Poisson solution presented in Figure 3.4.1-1. The comparison reveals that the two solutions do generally agree on the material's properties, specifically the bandgap is very similar. Therefore, the transition energies will be much more comparable than the individual confinement energies. This shows that the Schrödinger-Poisson solution used is reasonable.

When the STM tip is in equilibrium with the sample material a local charge transfer occurs to enable the Fermi levels of the metal and semiconductor to become equal this process is depicted in figure 2.3.2-1. The local contact potential between the tip and sample is what gives rise to the rectifying properties of the tip-semiconductor junction. From the voltage dropped across the tip-semiconductor junction the Fermi level shift can be measured and hence the positions of the eigenstates be adjusted to correct for this.

The tunnelling current as described in equation 2.1 is a function of barrier height φ, the barrier height is different depending upon the eigenstate being tunnelled into or out of. And so the rate of tunnelling into or out of a certain eigenstate is a function of its energy with respect to the Fermi energy.

It is important to note, however, that the applied bias V is not entirely dropped over the tip-sample interface.

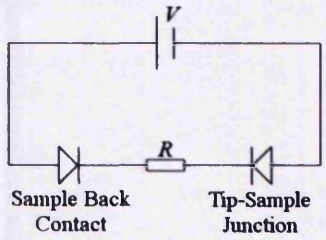

Figure 3.4.1-2: Model of STM voltage drop.

Figure 3.4.1-2 shows a model of how the applied bias V is dropped over the STM system. The sample back contact is shown here as a rectifying Schottky contact, however, if a suitable contact is made an ohmic contact may replace this. The resistor R denotes the impedance of the semiconductor sample and the tip-sample junction and back contact drop the remaining electrical potential difference. If the back contact was an ohmic or very near ohmic contact then the system simplifies to a resistance and a tunnelling junction.

From Ohm's law,

$$V\text{-}V_J=IR \qquad 3.3$$

Where V_J is the electrical potential dropped across the tunnelling junction and I is the tunnelling current.

In order to correct the voltage axis of the data it is important to know where the voltage is going at any point to predict the real voltage drop and build a model of $V_J(V)$.

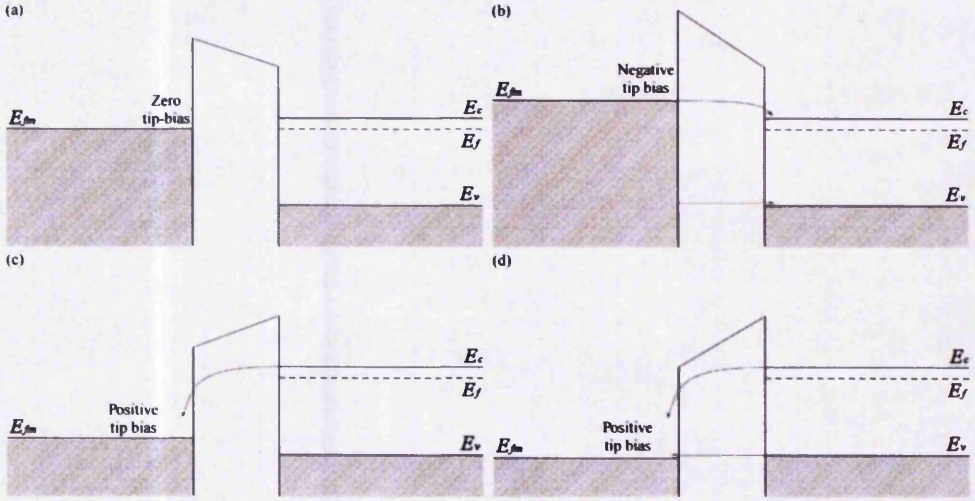

Figure 3.4.1-3: Flatband diagrams of tunnelling current at various applied biases.

Figure 3.4.1-3 shows flatband diagrams showing tunnelling of electrons into and out of the semiconductor from the tip; (a) shows zero bias, the potential drop is the contact

potential or built-in potential, (b) shows a negatively biased tip with electrons tunnelling into the conduction and valence bands of the semiconductor, (c) shows moderate positive tip bias able to overcome the contact potential and so allowing tunnelling from the conduction band of the semiconductor to the metal tip, and (d) shows a larger positive bias in which electrons from the conduction and valence bands are able to tunnel into the metal tip. The metal tip is assumed to be a continuum of states filled up to the Fermi level. When tunnelling into the conduction and valence bands of a quantum well (confined in one dimension) the lowest states into which the electrons can tunnel in negative bias and tunnel from in positive bias are above the band edge energy by the confinement energy. An effective bandgap of 1.64eV and 1.55eV is realised for the narrow and wide wells respectively.

The work function of tungsten is 4.6eV and the electron affinity of GaAs is 4.07eV, so the barrier height between the two materials is 0.53eV.

The *I/V* plot appears to straighten out in figure 3.4-6, this is usually the result of the ohmic part of the signal becoming more dominant, at large applied biases the tunnelling junction appears to be an ohmic interface with a small voltage offset. The dominating impedance governing the *dV/dI* value is that elsewhere in the system, so it is possible to estimate this impedance and remove the corresponding voltage drop from the voltage scale. The new voltage scale of applied bias should more accurately indicate the tip-sample junction bias.

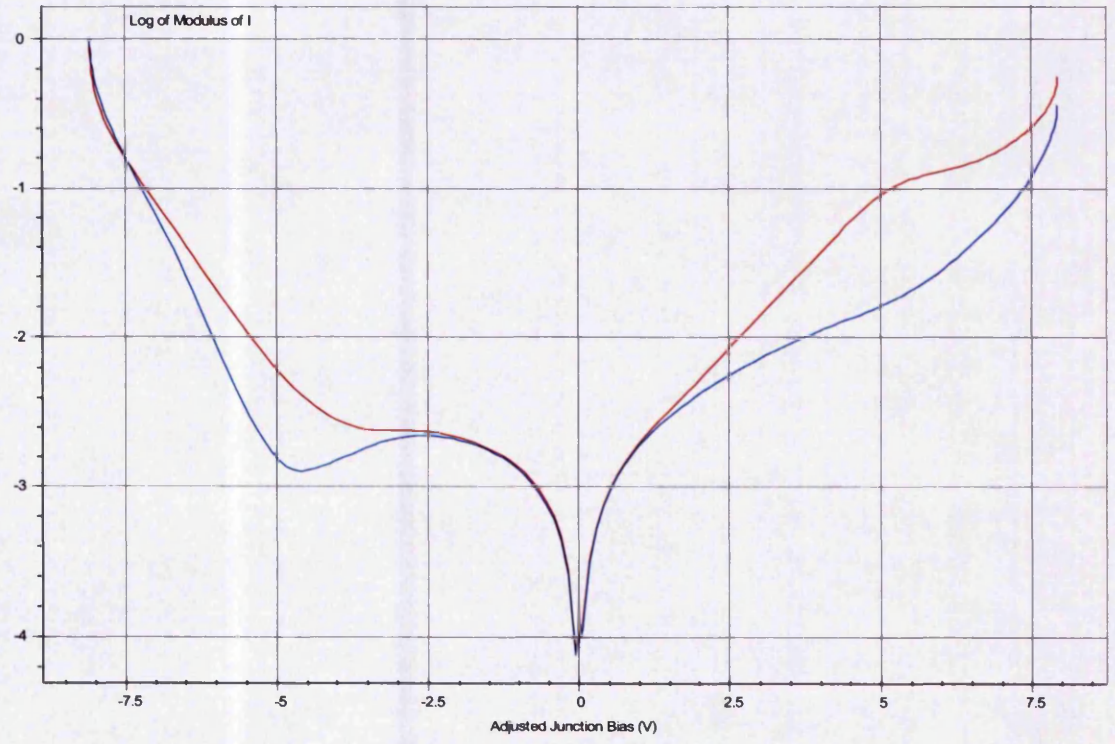

Figure 3.4.1-4: Log plot of modulus of I versus adjusted voltage scale.

Figure 3.4.1-4 shows a log plot of the modulus of tunnelling current against the adjusted bias voltage. The bias voltage is $V_{adj}=V-IR$, where R is $4\times10^{9}\Omega$ for positive applied bias and $1.4\times10^{9}\Omega$ for negative applied bias, these values are taken as the gradient of the original *I/V* curve straightens out at its endpoints. These values are confirmed by the asymptotic behaviour of the new *I/V* relationship at its limits. The effect of this correction is to proportionally scale the voltage downward to create a closer value to that dropped by the tip-sample junction.

This correction is not complete since it does not appear to account for the majority of the discrepancies in the applied potential, the correction is more effective at higher biases since it is dependant upon current, it does not correct for voltage lost when the tip bias is low.

Figure 3.4-8 shows a significant peak at +6V tip bias in the wide well *I/V* curve, this corresponds to the 2-DEG formed in the wide well where a significant number of electrons exist due to the behaviour of this material when illuminated. Beyond this region to a more positive tip bias, tunnelling out of the valence band becomes more dominant and the curves approach an ohmic like constant value.

It is expected that the increased tunnelling current in the wide well compared to the

narrow well at positive applied bias as depicted in figures 3.4-6 to 3.4-8 would commence when the applied bias overcomes the contact potential thus allowing the transfer of electrons from the wide well conduction band into the metal tip. Figure 3.4-8 shows this as a peak at +4V tip bias, a lack of a similar density of electrons in the narrow well causes no equivalent peak to be present on the blue curve. The second peak, peaking at +9V on the red line in figure 3.4-8 is thought to be the onset of the valence band edge tunnelling. For the same figure at -3V to -4V tip bias a dip in the current occurs, this can be accounted for as the rising barrier height caused as the junction enters reverse bias operation. Since the barrier is effectively rectangular, with a triangular top when biased, and the semiconductor side is pinned by being grounded, as the tip bias is increased the average barrier height will increase at half the rate of the tip bias change. Eventually the reverse biasing overcomes the barrier and tunnelling commences, peaking for both wide and narrow wells between -6V and -7V tip bias. The narrow well (blue) tunnels more readily at this point than the wide well (red), this is attributable to the availability of hole states in the valence band of the narrow well and that the conduction band of the wide well is already partially populated with electrons.
The quoted tip biases are those applied to the entire system and the voltage dropped across the tunnelling junction in not accurately known due to an unexplained non-ohmic voltage drop elsewhere in the system.

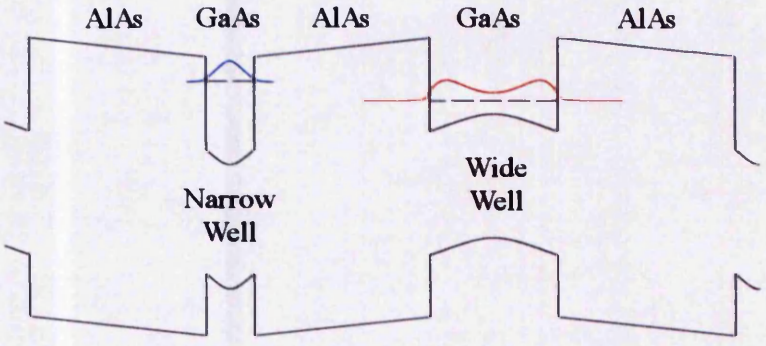

Figure 3.4.1-5: Electric field induced band bending between material layers.

One possible cause for the apparent increased tunnelling toward the edge of the wide quantum well is the effect of band bending caused by the large numbers of charges (electrons and holes) into the wide and narrow wells. The result of this charge is a distortion of the wells and a resultant augmentation of the eigenfunctions, such a distortion was reported by Galbraith *et al* for the heavy hole subband[2]. The lowest energy positional probability may be partly inverted resulting in an increased probability near the well edges. The narrow well would undergo the opposite effect and the distribution would be enhanced in the middle of the well, as would the holes in the wide well. These changes would be difficult to detect since they are just enhancing an effect that is already expected. Figure 3.4.1-5 shows the effect of the electric field between the wells and the resultant augmentation effect on the ground state electron probability distributions. It is necessary to know the voltage drop over the barriers to understand the scale of this effect, the system can be simplified to a parallel plate capacitor with a capacitance C, an area A, a plate separation d and a permittivity ε_s which is $12.9\varepsilon_0$.

$$C = \varepsilon_s \frac{A}{d} \tag{3.4}$$

If substituting $C=Q/V_{gap}$ and rearranging gives,

$$\frac{V_{gap}}{d} = \frac{Q}{A\varepsilon_s} = E \tag{3.5}$$

which is the electric field, and since the charge on the capacitor Q per unit area A is simply the number density of electrons multiplied by the elementary charge then,

$$V_{gap} = d\frac{N_d e}{\varepsilon_s} \tag{3.6}$$

Using values of d = 93Å and $N_d=5\times10^{11}\text{cm}^{-2}$ from Ref. 2 gives a voltage V_{gap} of 0.07V.

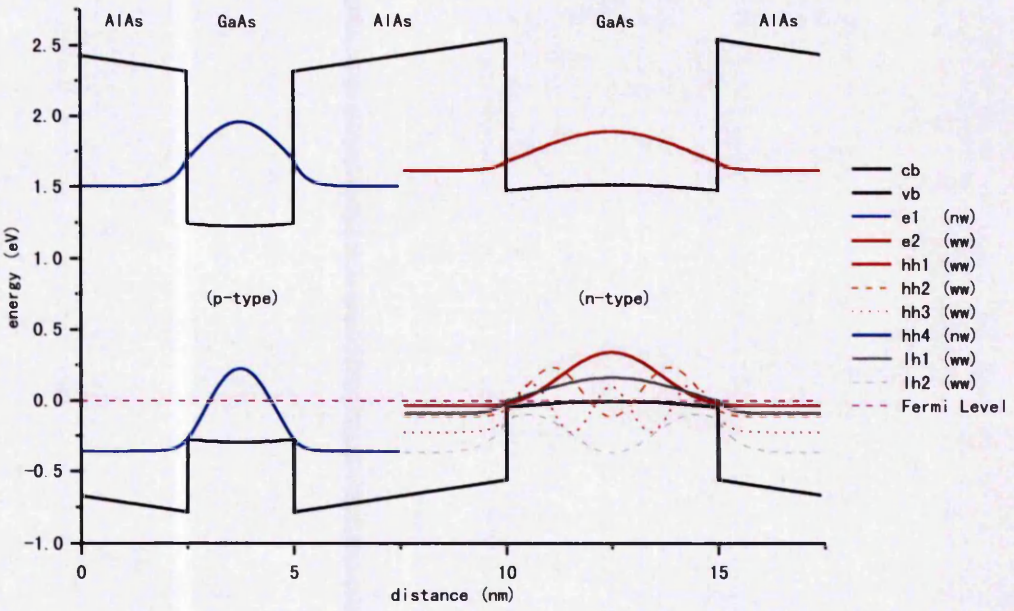

Figure 3.4.1-6: Calculated effect of electric field on electron and hole positional distributions.

Figure 3.4.1-6 shows the result of a numerical calculation[9], which reveals that an electric field equal to that previously calculated will not distort the ground state electron positional probability distribution enough to be the cause of the observed phenomenon. The calculation used an ion doping profile to create the electric field across the barrier. By injecting holes and an electrons into the narrow and wide wells respectively the electric field is created. However, the real electron and hole populations which cause the electric field are distributed themselves within the wells by their positional distribution function, which, in turn is being distorted by the electric field. This recursive process will reach an equilibrium not calculated here. It is, however, reasonable to assume that the small effect calculated would not give rise to a large effect with a second or third order calculation.

Galbraith *et al.* noted that with one set of materials this skew effect caused resonant hole tunnelling from the narrow well to the wide well as two eigenstates were brought into the same energy level, this significantly limited the maximum charge separation achievable[2]. The material used in this research, however, is of the next generation and was designed to avoid this resonant hole tunnelling problem and so a higher charge separation can be achieved[2,10]. that well, however, the data available may not contain enough resolution to detect smaller features or augmentation if they existed.

The shape of the narrow well is easily described as the single electron eigenfunction available in that well, however, the data available may not contain enough resolution to detect smaller features or augmentation if they existed.

Alternately the double peak from figure 3.4-5 may be explained as a superposition of wavefunctions. Figure 3.4-4 shows the wells and a clear contrast within the wide well material. The relative sizes of the peaks are indicative of the difference in the energy of their eigenstates and hence tunnelling probability. Indeed confined electron wavefunctions have been previously imaged in STM notably by Grandidier *et al.* who demonstrate electron confinement in quantum boxes[10].

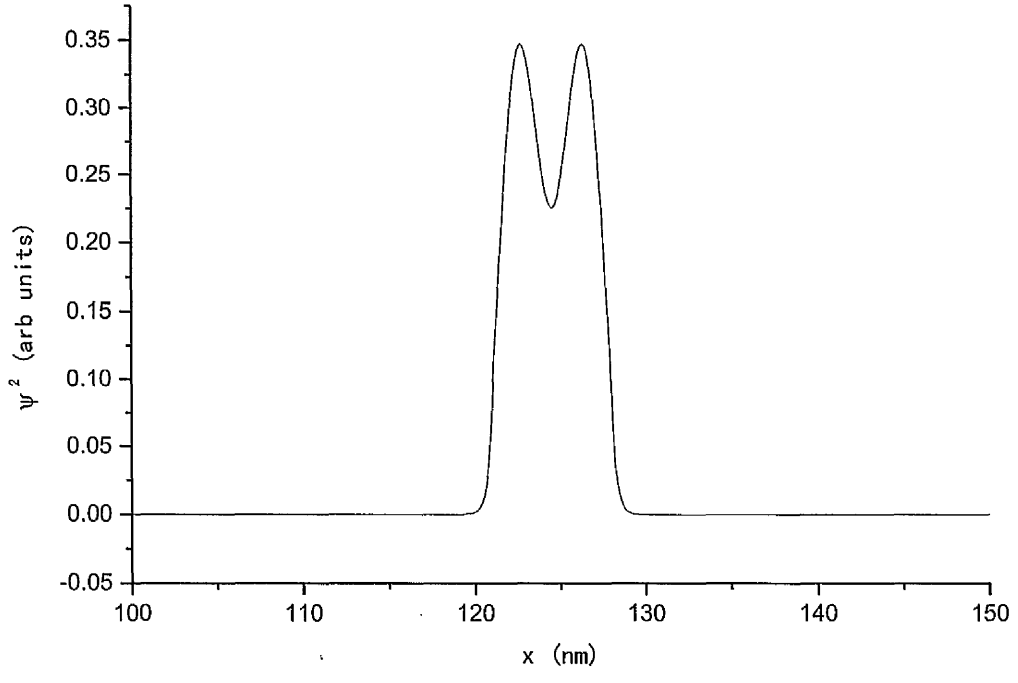

Figure 3.4.1-7: The sum of the first two electron eigenfunction probability distributions in the wide quantum well.

Figure 3.4.1-7 shows the simplest model of superposition of electron wavefunction probabilities. The probability distribution for the 1st and 2nd electron eigenstates are added together. While there are similarities with the peaks in figure 3.4-5 it is a poor model and does not explain the relative peak sizes. This model also does not explain the observed asymmetry in the well, this is thought to be a skew in the data since the background level also appears to be skewed.

Another factor is affecting the relative components of the 1st and 2nd eigenfunctions in the superposition as the measured wavefunction in figure 3.4-5 has a much less significant 2nd eigenfunction component.

At a temperature T the Boltzmann distribution for a discrete state system is given by,

$$P_i = \frac{e^{-\frac{E_i}{kT}}}{\sum_i e^{-\frac{E_i}{kT}}} \qquad 3.7$$

where P_i is the probability of the electron being in state i, E_i is the energy of state i and k is Boltzmann's constant. The sum at the bottom of the main division in the equation is a normalisation factor to force the sum of all probabilities of being in any of the states in the system to be 1.

The confinement energies of the 1st and 2nd electron eigenstates for the wide quantum well places virtually all of the electrons into the 1st eigenstate since the confinement energy of 68meV for the 1st eigenstate is larger than the 6.64meV value for kT but the confinement energy of the 2nd eigenstate is 239meV, which is considerably larger than the value for kT. The probability of an electron being in E_1 at this temperature is virtually 1.

The Boltzmann distribution does not explain the observed ratio as well as a simple summation distribution, however, at this temperature virtually all electrons already present in the 2-D continuum of the quantum well will be in the ground state (lowest eigenstate) and so this is not a simple 2 state system but a partly filled subband. This partly filled subband reduces the availability of lowest energy states and so the next available subband is the second eigenstate. This will change the relative eigenstate occupation probabilities for the final state of electron tunnelling. The behaviour of this material when illuminated will give rise to a large occupancy of ground state electrons in the wide quantum well.

The tunnelling current I_t between the tip and sample is a function of the transmission coefficient T_c, the density of states g of both the tip and sample, and the electron wavefunction ψ. Although the part of the wavefunction is often ignored in the simple free electron models often presented. In the case of the quantum wells the 2 dimensional confinement gives a density of states function which is a constant at 0K, this is given by

$$g = \frac{m_{eff}}{(\pi \hbar^2)} \qquad 3.8$$

where, in the case of GaAs $m_{eff} = 0.067m_0$ and m_0 is the free electron mass. This leads to a density of states of 2.79×10^{13} $eV^{-1}cm^{-2}$. In the interval between the first and second state (0.172eV) there exists $4.79\times10^{12}cm^{-2}$ available subband states. From the optical absorption the number of carriers generated can be given by

$$n = \frac{\alpha \tau I_i \lambda_i}{hc} \qquad 3.9$$

Where α is the absorption coefficient, τ is the carrier lifetime, I_i is the incident light intensity and λ_i is the incident light wavelength. The absorption of interest is the narrow quantum well as this is the generator of carriers with long lifetimes. The excitation in the wide well does not contribute significantly to the equilibrium carrier density in the well and can largely be ignored since the recombination lifetime is so short[3]. At light wavelength 632.8nm (1.96eV) α is approximately $8\times10^5 cm^{-1}$ from Casey *et al.*[12] and given the narrow well width of 2.5nm the absorption ratio becomes 0.2. The recombination lifetime τ of the Γ–X–Γ scattered electrons is a few microseconds[2], for this calculation τ = 5μs. Our incident light intensity I_i is $1 Wcm^{-2}$. This yields an equilibrium carrier population in the wide well of $n = 3.19\times10^{12} cm^{-2}$. Given the estimation of the value for recombination lifetime could be double or even triple the value used the carrier density created by the laser could easily saturate the available states in the wide quantum well from the first subband to the X state in the barrier leaving energy states from the X state to the second subband and equal energy states from the first and second subband into which to tunnel. If the states are filled by the Γ–X–Γ transfer mechanism then the limit of filling is the X state energy level, which is below the second electron state in the wide well but above the first. The result is a partially filled first subband from E(n=1) to E(X). The X state is 0.174 eV above the conduction band edge for the wells.

E(X)-E(n=1)=104meV which gives an areal carrier density of $2.90\times10^{12} cm^{-2}$ from equation 3.5. Thus the remainder of available n=1 states is 239meV - 174meV = 65meV which gives an areal carrier density of $1.81\times10^{12} cm^{-2}$.

Kirchhoff's first law states that the currents flowing into a junction equal those flowing out of the junction. In the case of the STM tip the measured current can be the sum of more than one simultaneous tunnelling route. In this case it is tunnelling into the n=1 subband and the n=2 subband, which can be considered separately and simply summed to produce the total observed current. Usually one tunnelling circuit dominates the observed tunnelling current; the one with least impedance.

At the midpoint in the well it is evident from the wavefunctions that the effect from the n=2 component is at its minimum and that from the n=1 component is at its maximum.

The tunnelling current can be given by,

$$I=\frac{4\pi Q_e}{\hbar}e^{\frac{-2z_t}{\hbar}\sqrt{2m\phi}}\int_0^{E_f} g_t(E)dE\,\Psi_t^2\int_{E_n}^{\phi} g_s(E)dE\,\Psi_s^2 \qquad 3.10$$

Where Q_e is the charge of an electron, z_t is the tip-sample separation, φ is the barrier height, $g(E)$ is the density of states function for the tip (t) and sample (s), and Ψ is the sample wavefunction. Since the STM tip is a metal the free electron model applies and there will always be a suitable state to tunnel to or from, therefore, the wavefunction distribution for the tip can be ignored by assuming it to be 1. The density of states of the tip is also unimportant, the metal tip is filled up to the Fermi level and a state to tunnel into or out of will always be available. For the sample, the density of states function is independent of energy for the 2-D confined system and so the integral becomes simply the product of the constant DOS function and the difference in energy from the lowest available state for that subband and the barrier height, which is defined by the applied tip-sample bias. Thus the tunnelling current can be reduced to,

$$I=\frac{4\pi Q_e}{\hbar}e^{\frac{-2z_t}{\hbar}\sqrt{2m\phi}}\gamma_s\Psi_s^2 \qquad 3.11$$

Where γ is $g(\varphi - E_n)$ or more simply the number of available states within the energy range. This equation can be evaluated separately for both n=1 and n=2 state tunnelling so that $I_{total}=I_1+I_2$ which can be factored to give,

$$I_{total}=\frac{4\pi Q_e}{\hbar}e^{\frac{-2z_t}{\hbar}\sqrt{2m\phi}}(\gamma_1\Psi_1^2+\gamma_2\Psi_2^2) \qquad 3.12$$

For both the 1st and 2nd tunnelling components. γ, which in the case of this material system is a staircase function, when broken down into it's components, does not make provision for energy levels below the confinement energy for each component, for which the available states is zero.

In these experiments I is kept at a constant value and z is varied to improve stability and reduce the occurrences of tip – sample contact. By taking the natural logarithms the equation can be rearranged to,

$$\frac{\hbar}{2\sqrt{2m\phi}}\ln\frac{4\pi Q_e}{I_{total}\hbar}+z_t=\frac{\hbar}{2\sqrt{2m\phi}}\ln(\gamma_1\Psi_1^2+\gamma_2\Psi_2^2) \qquad 3.13$$

where the first part of the left hand of the equation (before the addition) is effectively a z_0 offset. And so for changing z, this constant can be ignored.

$$\Delta z_t=\frac{\hbar}{2\sqrt{2m\phi}}\ln(\gamma_1\Psi_1^2+\gamma_2\Psi_2^2) \qquad 3.14$$

Equation 3.14 shows the relationship between varying tip-sample separation and

specifically for this analysis the two eigenfunctions and areal carrier densities. This result is comparable to that proposed by Song *et al.*[13] In order to calculate the relative magnitudes of the observed features known limits must be considered. The magnitude of the *z* deflection is mostly dependant upon just the n=1 eigenstate in the middle of the quantum well where the normalised wavefunction distribution becomes one for this state and zero for the n=2 eigenstate.

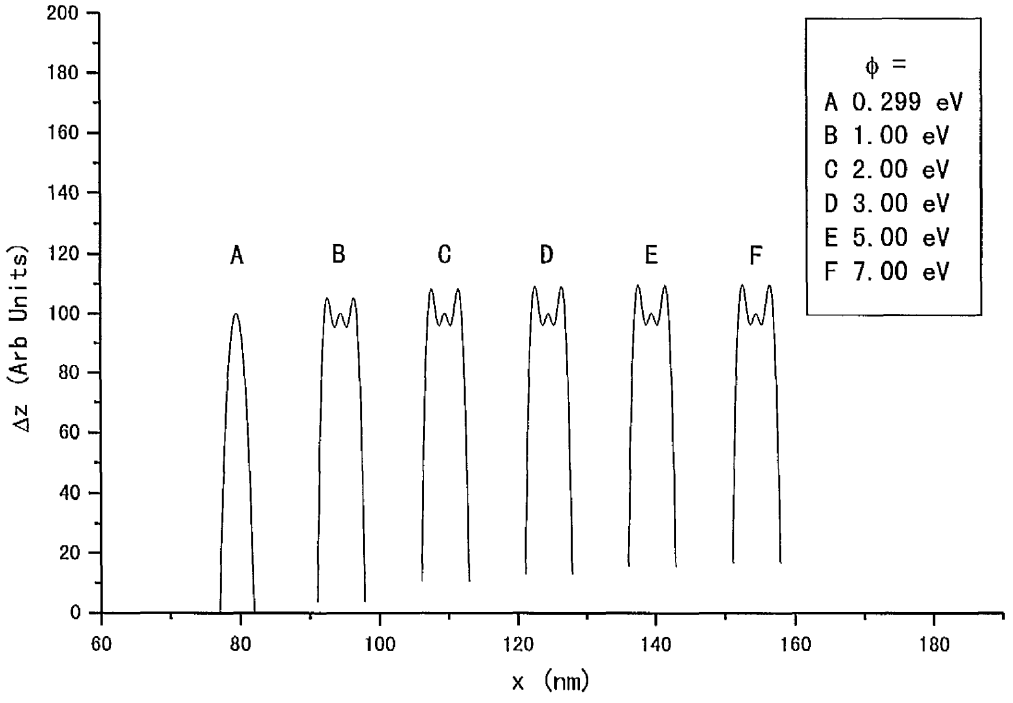

Figure 3.4.1-6: Combined Δz response for constant current mode scanning of wide quantum well structure for various values of φ.

Figure 3.4.1-6 shows a set of Δz responses, calculated by passing the normalised wavefunctions of the n=1 and n=2 states through equation 3.14. Noting that γ has a dependence on φ it is clear that when φ is equal to the n=2 energy level, A in figure 3.4.1-6, there is no component from the second energy level. However, as φ is increased, the characteristic ratio of the second to first eigenstate components becomes apparent. The apparent raising of the baseline as φ increases is an artefact of cropping the data at the edge of the quantum well, as the second eigenfunction becomes more significant the effective curve is broadened and since the data points are discrete they are clipped at ever higher values. The bump in the middle of the well indicates that the

second eigenfunction is not equal to the first, and indeed can never be. However, as φ increases their ratio will shift so that the relative height of this bump is vanishing. This bump is not clearly visible in figure 3.4-5, however, it could easily be obscured by noise; although the 3rd complete wide quantum well from the left of figure 3.4-5 does have some evidence of a flattening or bump in the middle of the well. The features presented in figure 3.4.1-6 are consistent over a broad range of φ, the same range in which the tip-sample bias is expected to be for figure 3.4-5. The features also fairly closely resemble those observed and depicted in figure 3.4-5.

3.5 Conclusion

The mixed type I – type II material is a truly novel structure allowing large spatially separated electron and hole plasmas to form with very little incident illumination. This unique property has allowed the development a method of photoenhanced STM of an indirectly formed electron gas and the successful characterisation of the material therein.

The material has been characterised and values found for well widths that closely mirror those used as the growth parameters. The wide wells are measured as 6.78±0.01nm, the narrow wells are 2.73±0.01nm and the barriers are 9.31±0.01nm, neglecting STM positional inaccuracies. Interestingly the subsequent treatment of the wells as a superposition of probability distributions allows for uncertainty in these parameters.

The STM will only measure electronic states into or out-of which electrons can tunnel, and since this process is elastic in nature it becomes possible to directly image and investigate electronic features with a certain energy level. It is then possible to image the wavefunction probability distribution directly and selectively.

An electron gas formed by the material when illuminated has been detected and imaged, although the exact position of the increased LDOS in applied bias is not clear as the voltage scale is not correctly represented, however, it is not unreasonable to suggest that it will be above the conduction band edge for the wide well.

The dependence of this phenomenon on illumination has been demonstrated through the use of locked-in photoenhanced STM.

3.6 References

1. J Feldmann, M Preis, EO Göbel, P Dawson, CT Foxon, I Galbraith, *Sol. St. Commun.* **1992**, *83*, 245.
2. I Galbraith, P Dawson, CT Foxon, *Phys. Rev. B.* **1992**, *45*, 13499.
3. P Dawson, I Galbraith, AI Kucharska, CT Foxon, *Appl. Phys. Lett.* **1991**,*58*, 2889.
4. Unpublished software provided by P Dawson, University of Manchester.
5. IH Libon, S Baumgärtner, M Hempel, NE Hecker, J Feldmann, M Koch, P Dawson, *Appl. Phys. Lett.* **2000**, *76*, 2821.
6. JA Stroscio, RM Feenstra, AP Fein, *Phys. Rev. Lett.* **1986**, *57*, 2579.
7. Jenkins, White, *Fundamentals of Optics*, **1957**, third edition, McGraw-Hill.
8. GFA van de Walle, H van Kempen, P Wyder, *Appl. Phys. Lett.* **1987**, *50*, 22.
9. S Birner, Nextnano3, Walter Schottky Institute, Technishe Universität München, *http://www.wsi.tum.de/nextnano3*
10. P Dawson, *J. Lumin.* **1992**, *53*, 293.
11. B Grandidier, YM Niquet, B Legrand, JP Nys, C Priester, D Stiévenard, *Phys. Rev. Lett.* **2000**, 85, 1068.
12. Casey, H. C., D. D. Sell, and K. W. Wecht, *J. Appl. Phys.* **46**, 1 (1975) 250.
13. HZ Song, M Kawabe, Y Okada, R Yoshizaki, T Usuki, Y Nakata, T Oshima, N Yokoyama, *Appl. Phys. Lett.* **2004**, *85*, 2355

Chapter 4: STM investigation of InGaN/GaN quantum well structures.

4.1 Introduction.

The nitride III-V group of materials has attracted a great deal of interest over recent years since the nitride based blue LED and blue-violet LD were invented. This led to the complete effective coverage of the visible spectrum by light emitting semiconductors, enabling the production of full colour LED display systems and improved optical data storage devices. This device potential has been previously correctly identified and attempts to manufacture device quality material the subject of much interest[1]. Maruska and Tietjen synthesised GaN thin films on sapphire using ammonia (NH_3) as a carrier gas for the nitrogen component and successfully produced single crystalline films, however, they noted that Zn and Mg p-type doping produces high resistivity material which is unsuitable for device production[1]. This early HVPE (Hydride Vapour Phase Epitaxy) laid the foundation for more advanced vapour deposition methods.

No native substrate exists for GaN growth[2] A significant lattice mismatch (~13.8%) between GaN and sapphire (Al_2O_3), the most commonly used substrate for device production, exists[1,3]. This lattice mismatch and the difference in the coefficient of thermal expansion between the two materials[4] causes a large crack density to form in the GaN during growth[3]. An AlN buffer layer was used to reduce crack density dramatically and provide high quality crystalline GaN films[3,5]. Subsequent growth of a GaN on a GaN buffer layer improved electrical characteristics over GaN on AlN buffer layer[6].

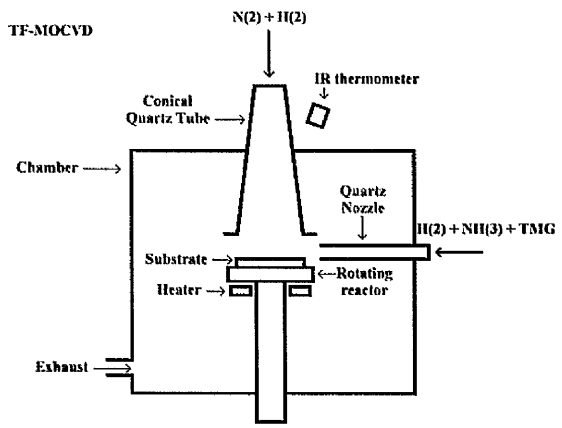

Figure 4.1-1: Nakamura's two-flow MOCVD reactor adapted from 5,6.

Nakamura *et al.* produced devices by a novel growth method involving a modified two

flow MOCVD reactor[5,6], GaN thin films grown on the (0001) C-plane of sapphire have been grown with uniformly high crystal quality. P-type doping of GaN involves the use of Mg as a dopant, however, as reported[1], the electronic properties of Mg doped GaN is highly resistive. LEEBI (Low Energy Electron Beam Irradiation) treatment after Mg doping was discovered to improve resistivity and hole mobilities of the material near the surface and allow prototype device production[7-9]. It was discovered that thermal annealing in a hydrogen free environment after Mg doping reduced the resistivity of the material from ~$10^6\Omega$/cm to 2-8Ω/cm and increased hole mobilities accordingly[10]. This improvement was not limited to the near surface material, however, is otherwise identical to the results produced by LEEBI treatment[10-11]. It was also observed that this process could be reversed[11]. Native GaN is conductive n-type, in order to achieve p-type conductivity enough p-type doping must be included to cancel out the native n-type carriers to achieve neutrality. It was suggest that native defects are formed with the magnesium within the GaN making p-type doping difficult, but also that in the hydrogen rich atmosphere of an MOCVD reactor that hydrogen forms acceptor-H complexes with the magnesium before defects are formed within the GaN and so replace the defects and subsequent annealing in a hydrogen free environment causes the hydrogen to leave the GaN crystal and the Mg in state without defects[11-13].

The material system involving Wurtzite GaN and it's ternary derivatives $Al_xGa_{1-x}N$ and $In_xGa_{1-x}N$ grown upon a sapphire substrate can produce a wide variety of optoelectronic devices despite the fact that the lattice mismatch between the material and it's substrate causes highly strained growth and cracking of the growing material. A dislocation density of 1-10^{10}/cm^2 has been reported[14]. In most material systems this high threading dislocation density would cause non-radiative recombination centres and would result in an inefficient device that fails rapidly due to overheating. In the $In_xGa_{1-x}N$ material system, however, the majority of the electron-hole pairs (excitons) recombine radiatively since it is thought that they are localised in the plane of the epitaxy and so do not reach the non-radiative recombination centres[15,16]. This leads to the high reported efficiency of $In_xGa_{1-x}N$ based LEDs and laser diodes[14,17]. The nature of this localisation has been the subject of much debate in recent research[17-22]. One theory to account for this localisation effect is that of clustering of the indium in the ternary compound $In_xGa_{1-x}N$ which composes the quantum wells in this system[17]. The suggestion that there

is a miscibility gap in the $In_xGa_{1-x}N$ component forcing the indium fraction to be either side of the gap and hence causing clustering[23], presents a challenge well suited to STM to resolve such a small size scale fluctuation of chemical composition ≤100nm scale and determine if it exists. Karpov suggests that elastic strain within the InGaN layers can suppress the phase separation and allow the chosen fraction to be miscible even though a miscibility gap exists for this fraction in bulk material[24]. However, Bangert *et al.* suggests although not for this specific material system that compositional fluctuations could be a mechanism for strain relaxation[25] and later provides evidence for compositional fluctuation on a length scale of ~20nm in InGaN quantum well structures in the form of STEM (Scanning Transmission Electron Microscope) images[21] this is in agreement with Chichibu *et al.*[15]. Liliental-Weber *et al.* also provide TEM and X-ray crystallography evidence for periodic indium segregation in InGaN grown on GaN and AlN buffer layers[26]. Interestingly Smeeton *et al.* showed that InGaN quantum wells are sensitive to the electron beam used in TEM, their results show that strain induced by the electron beam causes damage which closely mirrors the results expected by nanometre scale indium concentration fluctuation[27,28].

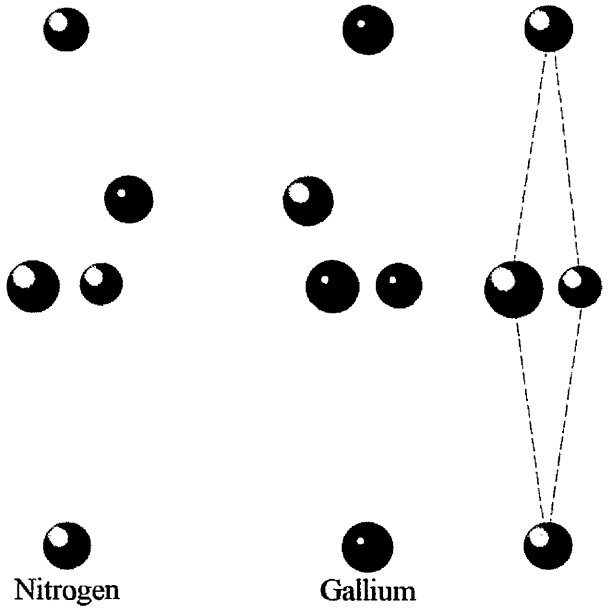

Figure 4.1-1: The Wurtzite crystal structure of GaN.

Figure 4.1-1 shows a single unit cell of the hexagonal Wurtzite crystal structure of GaN, the dashed lines join a set of nitrogen atoms in-plane with each other, the same applies for the gallium atoms behind. Only the two offset atoms in the top left quadrant of the diagram are not in the same plane as other atoms in this single unit cell. They are in the

same plane as a set of atoms in the greater crystal bulk. Another two offset atoms should appear in the quadrant below, however, they are omitted as they do not form part of this unit cell. In $In_xGa_{1-x}N$ or $Al_xGa_{1-x}N$ materials indium and aluminium atoms are substituted in place of gallium atoms by proportion of the ratio x. The hexagonal nature of this crystal structure is only visible with three or more unit cells.

A set of five material samples were used for this research, they are ten period structures of 2.5nm $In_xGa_{1-x}N$ quantum wells and 7.5nm GaN barriers grown on a 2.5μm buffer layer on a sapphire substrate. There is no capping layer. The five samples differ in indium fraction from five percent to twenty five percent inclusive in incremental steps of five percent. These material samples were grown using a Thomas-Swan 6 × 2 in. close-coupled shower-head MOCVD reactor. These samples have a visibly yellow tint to them under normal lighting conditions, the amount of this tint is proportional to the indium content in the quantum wells, with the 25% indium fraction well being the most tinted.

4.2 Objective

The objective of the research into this material is to identify the quantum well structures with STM and investigate the nature of the localisation by looking for localised fluctuations of the indium fraction within the wells. Spectroscopic measurements should be able to detect the different chemical composition and if one exists.

4.3 Method

Preliminary STM tests were performed on the epitaxial surface of a GaN film grown on sapphire, the surface was cleaned using water and acetone and mounted onto a flat steel sample plate using silver loaded epoxy glue. As the substrate is sapphire the glue was allowed to bridge the material's surface to the sample plate in order to permit a conducting path.

Various cleaving techniques were tested on these materials, conventional cleaving is not possible with this material since the large lattice mismatch between the GaN and the sapphire substrate does not guarantee a cleavage plane can be found by cleaving the substrate. Indeed there are some suggestions that sapphire can not be cleaved in the traditional sense[29]. Sapphire is a very hard material, Al_2O_3 in powder or particle form is used extensively as an abrasive since it is much cheaper than diamond and just as effective in most applications. Sapphire has a number of cleave planes with roughly equal strengths only a slight perturbation is required during cleaving to cause the crack to change direction. The brittle and often unpredictable nature of sapphire cleaving attempts led to the development of a simple but effective way of controlled breaking of the substrate. The non-ideal breaking of the substrate material as opposed to cleaving is not necessarily an issue. As has been experienced with other materials, if a crystal is broken or poorly cleaved in a plane similar to that of a crystal plane then large investigable regions of material are present interrupted by crystal steps, which allow the edge to approximate the breaking plane. The technique used was designed to preserve a region of material while breaking off any excess. A lever was used to create the breaking force by moment and a secondary force was used to direct the crack propagation along the material's length. This approach could control crack propagation in most cases. The resultant material edge would occasionally appear very flat under optical microscopes, however, the nature of the sapphire and GaN makes contrast very poor with conventional optical microscopy.

Once the material's edge was prepared it was mounted vertically for X-STM investigation onto a stainless steel toothed sample plate using silver loaded epoxy in the same manner as depicted in figure 2.3.2.5-1. The STM investigation of the material edge was conducted. Standard STM tip auto approach systems are not suitable for use

with this material as the substrate, sapphire, is an electrical insulator. The STM tip will not sense any tunnelling and will continue to approach until the tip has crashed and buckled.

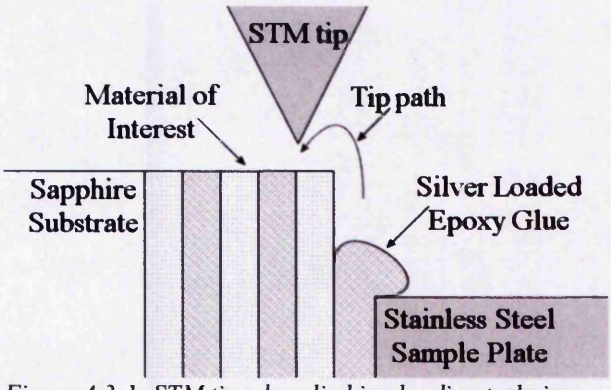

Figure 4.3-1: STM tip edge climbing landing technique.

STM tip approach was performed manually using an edge climbing technique. The tip was targeted slightly over the GaN edge and the standard auto approach was initiated. Once the tip was clearly over the edge and a tunnelling current detected (from the side of the tip) the tip could be retracted and moved inward toward the sample's substrate until no tip retraction is necessary to maintain a continuous tunnelling current during lateral (toward substrate) motion. At this point the material's edge is located. With these samples there is no capping layer so the immediate edge is the edge of the quantum well structure.

Atomic Force Microscopy techniques were also used to investigate this material's edge morphology and conductivity. The sample was mounted in the same way as for STM the AFM probe was landed on the cleaved or broken sapphire substrate since conduction is not a requirement for AFM. Some topographic images of the sapphire cleaves were obtained for comparison with cleaving of other materials. The probe was gradually moved toward the sample's edge until it was detected. In this region material morphology was investigated and conducting AFM (CAFM) performed.

A novel method was developed to investigate the cross sectional features using the standard top down arrangement for STM and AFM.

4.4 Results

Surface STM revealed interesting surface morphology consistent with a cracked material growth. The uneven surface morphology appears to be isotropic and the presence of dislocations and other crystal defects could account for this. The observation of grains was noted.

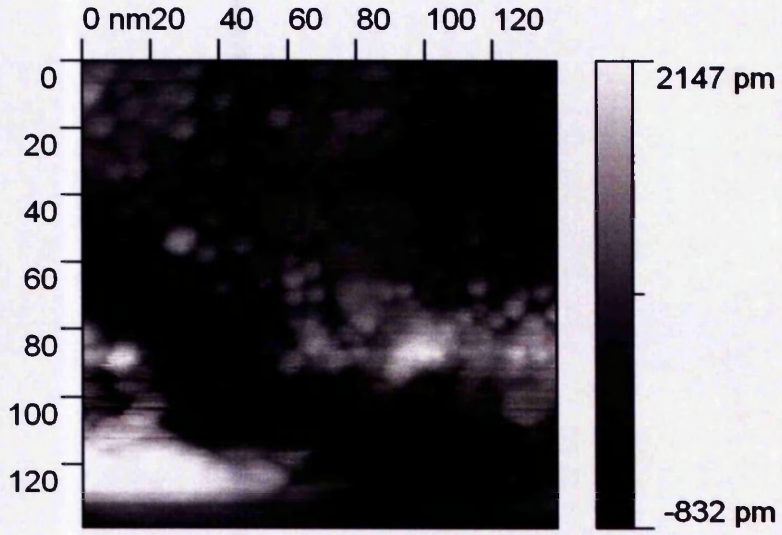

Figure 4.4-1: STM of GaN surface, grains visible.

Initial *I/V* spectroscopy revealed the wide band-gap of the material and that it is n-type.

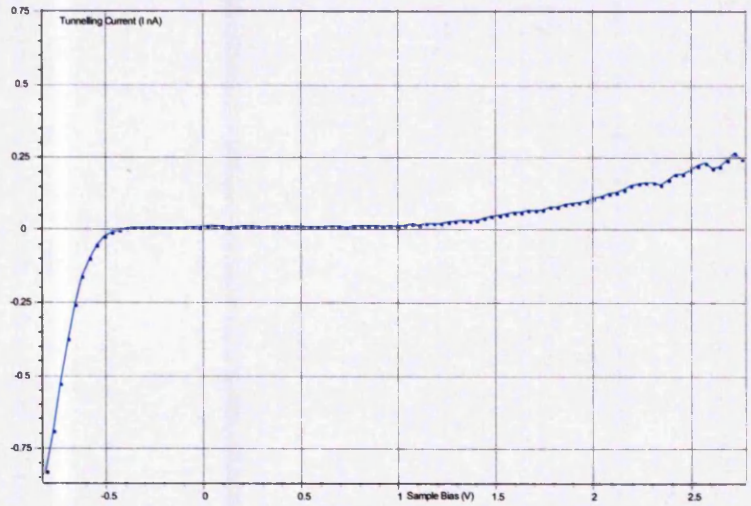

Figure 4.4-2: I/V spectroscopy taken on GaN surface, note the position of 0 bias.

This result is consistent with the knowledge that GaN is intrinsically n-type[7].

The 25% indium fraction multiple quantum well sample was mounted for X-STM as shown in figure 4.3-1, the edge climbing procedure appeared to allow tunnelling and for

the STM tip to ascend the surface layer to reach the cross sectional region, however, it was discovered that the rise to the edge was not as abrupt as was expected, the GaN material appeared to taper inward toward the substrate so that when the top was reached there was no quantum well material left to investigate. The remaining GaN material was so uneven that scanning was not permitted since the feedback loop could not compensate for the changes in surface morphology effectively. An attempt was made to access the edge material using AFM to better understand the morphology and to perform conducting AFM.

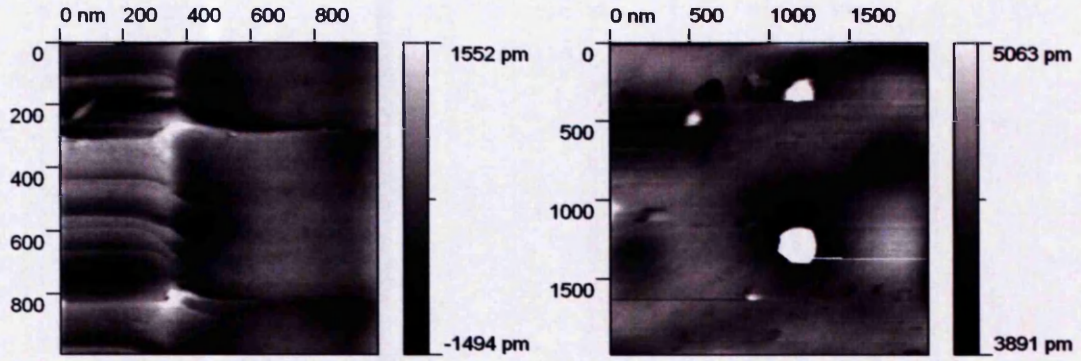

Figure 4.4-3: Broken sapphire substrate imaged by AFM.

The morphology of the broken sapphire substrate seemed to be locally very flat with the occasional large features, however, a continuous slope suggests that the break was not completely orthogonal to the surface, the slope has been removed from the data in figure 4.4-3 to enable contrast of smaller features.

In order to perform conducting AFM the AFM tip needs to be coated in a metal film, this was performed by evaporative coating as described in chapter 2.5.2 and depicted in figure 2.5.2-2. Initially gold was used to act as a conducting layer, it is an excellent conductor and is very unreactive.

While conduction was detected it seemed to fade quickly until no current was observed. Charging was excluded as a possible cause for this since the current would have returned by moving the probe to a different location. A test contact with an exposed metal part of the sample plate revealed the circuit was open. It appears that the gold layer had been removed by wear with the sapphire and GaN materials. The probe was re-coated in a platinum 80% iridium 20% alloy, since it is significantly harder than gold. The Pt-Ir alloy was also removed by the frictional forces between the tip and sample. It was also noticed that the resolution of surface topography was diminishing

throughout the experiments. As has been previously mentioned in chapter 4.3 sapphire is a very hard material, it is rated 9.0 on the Mohs scale of hardness. In real terms this is significantly harder than silicon (from which the AFM probe tip is produced) and is causing significant wear to the tip.

An attempt was made to image a GaN LED structure grown on silicon to gain insight into the properties of the material in a cross sectional orientation, silicon has known cleavage planes but is less well suited for crystal growth of GaN than sapphire. The silicon appeared as expected for medium resolution imaging, fairly flat with regions of steps on the surface. The edge material however, had the same problems as with sapphire, the material was not cleaved but appeared to be very uneven so as to inhibit scanning.

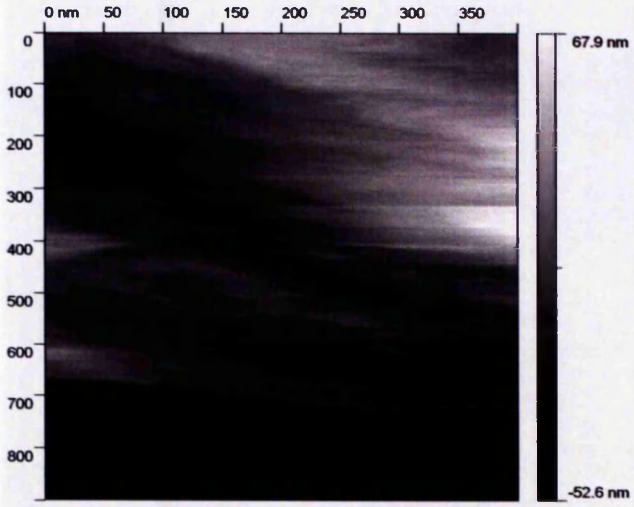

Figure 4.4-4.: Edge material of GaN on Si device.

Figure 4.4-4 shows STM image of GaN edge on Si, the dark region at the bottom of the image denotes the edge of the material (free space). Approximately 1μm of slope from the top to the bottom of the data was removed from the image to allow feature contrast, besides the slope surface roughness is still over 100nm. Note the image is not square but has an approximate 1:2 aspect ratio.

It appears as though the GaN layers are not cleaving with their substrate but are breaking in an unpredictable manner, this is not unexpected since there is a large lattice mismatch between these layers and any substrate used which produces a large threading dislocation density throughout the material[3,5]. During breaking sapphire requires a significant force to break the bonds within the material, this break, like a cleave is not a gradual process, the stress builds up to a point at which an entire shearing of layers

occurs ideally along a cleavage plane. The mechanical properties of sapphire mean that a large amount of energy is stored within the bonds of the substrate before breaking and at the moment of breaking this energy is released. It is possible that this release of energy is damaging to the epitaxial layers at the break point.

Figure 4.4-5: TEM image of GaN edge, from 24.

Figure 4.4-5 is a TEM image of InGaN on GaN on Sapphire[26], the material interfaces are uneven and dislocations run through the layers seeding at the interfaces.

Imaging of quantum wells usually requires exceptionally flat surfaces as noted in chapters 2 and 3, small amounts of topographic change render the electronic information invisible to the STM which has a finite (although wide) dynamic range on sensitivity and feedback loop control of the tip becomes less accurate the greater the topographic change. Reasons for this include overshoot, reduced resolution due to rescaling of the ADC (Analogue to Digital Converter) and positional drift caused by creep in the piezoelectric motors, the effect of which is proportional to the range of motion.

An alternative approach was devised to gain access to the cross sectional information. This method addressed the problems of placing an STM tip on the active material and the material quality upon landing. The method also offered the potential to enlarge the scale of the features being investigated in one dimension.

The method involved bevelling the sample at a very shallow angle from the normal surface effectively cutting through the active material. The material was mounted substrate down onto an angled lapping block with a gradient of 0.020 which had the effect of extending the feature sizes from 2.5nm wells and 7.5nm barriers to approximately 125nm wells and 375nm barriers, albeit with a shallow gradient. The

bevel cut through all of the material layers and into the substrate. The sample was large enough that there was a large region of non-bevelled surface. The newly mechanically formed surface would be roughened by the mechanical wear, so it was necessary to chemically etch work damage away and provide a region of smooth surface for STM. The surface was etched in a 10% by weight solution of NaOH in ethylene glycol at a temperature of 178°C for 45 seconds. This process has no observed directional etching preference[30]. An aluminium spot was evaporated onto the remaining epitaxial layer to act as an ohmic back-contact as aluminium is known to make a reasonably good ohmic contact with GaN[31,32].

Optically the newly formed facet appeared flat with a slightly rounded edge to the epitaxial surface. Interference fringes were visible under an optical microscope, formed by the material layers. As the layers thinned the fringes changed in a similar way to a Fabry-Perot etalon. The fringes appeared to be uniform along the bevel suggesting a fairly even facet. Also visible was the indium fraction related yellow tint, which visibly tapered off over the facet-epitaxial surface interface region. The presence of this tint indicated that the quantum well layers were intact. This allowed a target region to be set.

STM was unsuccessful on this material. No tunnelling current could be achieved on the facet or on the remaining epitaxial surface. Subsequent *ex situ* conductivity measurements confirmed that the surface was electrically inert. High (normal) levels of conductivity were noted however, on the edges of the material normal to the epitaxial layer. The aluminium spot showed no conductivity to any other part of the material including the edges. Work damage could result in an electrically inert surface but this would not explain the lack of conductivity on the epitaxial surface. The chemical etch process could be responsible for the damage although it is not understood how. Etching is essential to present a smooth surface, since the mechanical process leaves a surface unsuitable for high resolution STM. Other possible surface contaminants include the oil used as an etching medium for suspension of the diamond paste, however, this should have been removed by subsequent cleaning with alcohol and acetone and there was no visible evidence of an oil film or contaminant layer.

Spontaneous formation of indium rich nano-structures has been observed on InGaN surfaces[33]. This process causes indium clustering near surface defects. If this same

process applied near threading dislocations in InGaN quantum wells could cause the exciton localisation believed to be the origin of high efficiency light emission in InGaN based light emitting devices.

Similar InGaN quantum dots have been produced by MOVPE (Metal-Organic Vapour Phase Epitaxy) by depositing a GaN layer and subsequently InGaN onto a sapphire substrate[34]. Strain during growth causes the spontaneous formation of indium rich islands which have a significant topographical component.

AFM on these InGaN quantum dot structures reveals indium rich islands with a wide lateral aspect ratio of approximately 6:1. The low density and apparently random distribution of these dots is observed and allows for clear identification.

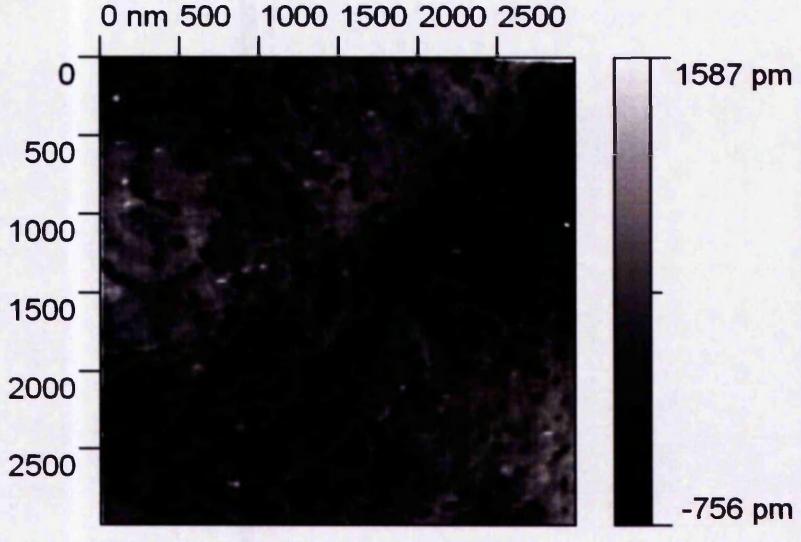

Figure 4.4-6: Indium rich islands on an InGaN layer.

Figure 4.4-6 shows the indium rich dots as bright spots on the flat InGaN surface. The dark regions are the surface expression of threading dislocations, they tend to open into a two dimensional Y pit formation (similar to the shape of a funnel) at the surface.

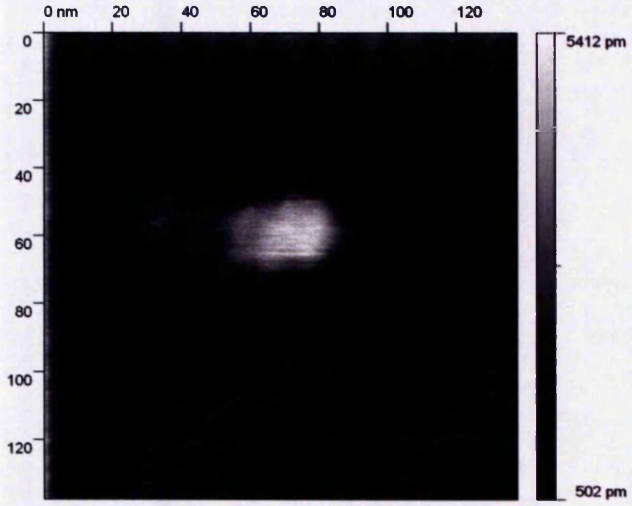

Figure 4.4-7: A double dot on the InGaN surface.

It has been noted that the dots tend to form in pairs more than might be expected by random coincidence, usually with one larger and one smaller. Figure 4.4-7 shows an AFM image of a double dot. The width of the main peak is approximately 30nm and the height above the surface is approximately 5nm. The wavy lines across the image are due to a mechanical vibrational source thought to be building vibration.

4.5 Conclusion

Although this research has failed to answer the indium clustering question it has provided direction for continued study that may provide an answer.

GaN is one of the most difficult semiconductors on which to perform cross sectional STM and there are no reports of this available, however, with further attention GaN could be imaged as a bevelled facet by either STM or the potentially more revealing SNOM (Scanning Near-field Optical Microscope) which operates in a similar manner to STM but uses light as the tip-sample interaction. SNOM uses the near field effect to overcome the diffraction limit that restricts the resolution of conventional optical microscopes and could look for localised luminescence and localised shift of luminescence spectra on a scale approaching the resolution achievable by STM, a bevelled sample would be more suitable for this method to improve lateral resolution.

It may yet be possible to perform STM on the bevelled facet, however, this will only be possible once the issue of surface conductivity has been solved. One group has reported cleaving GaN on sapphire[36], however, the surface roughness reported is of the order of 100 times larger than that required for STM investigations of quantum well structures and chemical composition.

InGaN does have a miscibility gap and will form localised indium fluctuations in bulk InGaN and on InGaN surfaces, however, these fluctuations have not been shown conclusively to occur in strained InGaN quantum well structures. Recently evidence to support the localisation theory has been published which suggests the localisation is on a length scale of ~2nm, although again the nature of the localisation is uncertain, evidence is presented to support the argument of localised well width fluctuations[35]. Another group has presented CFM (Capacitance Force Microscopy) data to support both well width fluctuations and indium concentration fluctuations, however, they have neglected to mention the possibility of surface charging caused by friction, which may explain why their CFM data closely maps the topography of their AFM data of the surface capping layer[37].

For now the question underlying the nature of localisation in InGaN quantum well structures and the high efficiency of the light emitting devices based upon this material remains.

4.6 References

1. HP Maruska, JJ Tietjen, *Appl Phys Lett.* **1969**,*15*, 327.
2. V Darakchieva, PP Paskov, T Paskova, M Heuken, B Monemar, Proc. 10th *EW MOVPE,* **2003**, *PS VII* 03.
3. H Amano, N Sawaki, I Akasaki, Y Toyoda, *Appl. Phys. Lett.* **1986**, *48*, 353.
4. WM Yim, RJ Paff, *J. Appl. Phys.* **1974**, *45*, 1456.
5. S Nakamura, Y Harada, M Seno, *Appl. Phys. Lett.* **1991,** *58*, 2012.
6. S Nakamura, *Jpn. J. Appl. Phys.* **1991,** *30*, L1705.
7. H Amano, M Kito, K Hiramatsu, I Akasaki, *Jpn. J. Appl. Phys.* **1989**, *28*, L2112.
8. S Nakamura, M Seno, T Mukai, *Jpn. J. Appl. Phys.* **1991,** *30*, L1708.
9. S Nakamura, T Mukai, M Seno, *Jpn. J. Appl. Phys.* **1991,** *30*, 1998.
10. S Nakamura, T Mukai, M Seno, *Jpn. J. Appl. Phys.* **1992,** *31*, L139.
11. S Nakamura, N Iwasa, M Seno, T Mukai, *Jpn. J. Appl. Phys.* **1992,** *31*, 1258.
12. JA Van Vechten, JD Zook, RD Horning, B Goldenberg, *Jpn. J. Appl. Phys.* **1992,** *31*, 3662.
13. J Neugebauer, CG Van de Walle, *Appl. Phys. Lett.* **1996**, *68*, 1829.
14. T Mukai, D Morita, S Nakamura, *J. Cryst. Growth.* **1998**, *189*, 778.
15. S Chichibu, K Wada, S Nakamura, *Appl. Phys. Lett.* **1997**, *71*, 2346.
16. J Bai, T Wang, S Sakai, *J. Appl. Phys.* **2000** *88*, 4729.
17. Y Narukawa, Y Kawakami, M Funato, S Fujita, S Fujita, S Nakamura, *Appl. Phys. Lett.* **1997**, *70*, 981.
18. S Chichibu, T Sota, K Wada, S Nakamura, *J. Vac. Sci. Technol.* B. **1998** *16*, 2204.
19. JS Im, S Heppel, H Kollmer, A Sohmer, J Off, F Scholz, A Hangleiter, *J. Cryst. Growth.* **1998**, *189*, 597.
20. A Vantomme, Mf Wu, S Hogg, G Langouche, K Jacobs, I Moerman, ME White, KP O'Donnell, L Nistor, J Van Landuyt, H Bender, *MRS Internet J. Nitride Semicond.* **2000** *5S1* W11.38.
21. N Duxbury, U Bangert, P Dawson, EJ Thrush, WV Van der Stricht, K Jacobs, I Moerman, *Appl. Phys. Lett.* **2000**, *76*, 1600.
22. H Chen, RM, Feenstra, JE Northrup, T Zywietz, J Neugebauer, *Phys. Rev. Lett.*

2000, *85*, 1902.

23. I Ho, GB Stringfellow, *Appl. Phys. Lett.* **1996**, *69*, 2701.
24. SY Karpov, *MRS Internet J. Nitride Semicond.* **1998**, *3*, 16.
25. U Bangert, AJ Harvey, VA Wilkinson, C Dieker, JM Jowett, AD Smith, SD Perrin, CJ Gibbins, *J. Cryst. Growth,* **1993** *132*, 231.
26. Z Liliental-Weber, DN Zakharov, KM Yu, JW Ager III, W Walukiewicz, EE Haller, H Lu WJ Schaff, *J. Electron Microsc.* **2005**, *54*, 243.
27. TM Smeeton, MJ Kappers, JS Barnard, ME Vickers, CJ Humphreys, *Appl. Phys. Lett.* **2003**, *83*, 5419.
28. TM Smeeton, MJ Kappers, JS Barnard, ME Vickers, CJ Humphreys, *Phys. Stat. Sol. B,* **2003**, *240*, 297.
29. B Mason, LG Berry, *Elements of Mineralogy*, **1968**, (Freeman, San Francisco).
30. DA Stocker, EF Schubert, JM Redwing, *Appl. Phys. Lett.* **1998**, 73, 2654.
31. JS Foresi, TD Moustakas, *Appl. Phys. Lett.* **1992**, *62*, 2859.
32. ME Lin, Z Ma, FY Huang, ZF Fan, LH Allen, H Moroç, *Appl. Phys. Lett.* **1994**, *64*, 1003.
33. JE Northrup, T Zywietz, J Neugebauer, *Phys. Rev. Lett.* **2000**, *85*, 1902.
34. B. Sherliker, P. Harmer, MP. Halsall, P. Buckle, PJ. Parbrook, T. Wang, *Microelectr. J.* **2005**, *36*, 223.
35. DM Graham, A Soltani-Vala, P Dawson, MJ Godfrey, TM Smeeton, JS Barnard, MJ Kappers, CJ Humphreys, EJ Thrush, *J. Appl. Phys.* **2005**, *97*, 103508.
36. DA Stocker, EF Schubert, W Grieshaber, KS Boutros, JM Redwing, *Appl. Phys. Lett.* **1998**, *73*, 1925
37. X Zhou, ET Yu, DI Florescu, JC Ramer, DS Lee, SM Ting, and EA Armour, *J. Vac. Sci. Technol. B* **2005**, *23*, 1808.

Chapter 5: Conclusion

Scanning tunnelling microscopy has proven to be an invaluable technique and is probably the single most important development in the field of nanoscale characterisation and manipulation. Its ability to directly image and map electronic and topographic information sets it apart from other microscopies.
Developments in SPM techniques including AFM and photoenhanced STM have widened the possibilities for various methods of material characterisation. By combining the highly localised nature of STM with other techniques, other properties of materials can be mapped such as the light dependence of tunnelling current as used in photoenhanced STM.

The characterisation of a mixed type I – type II multiple quantum well material has demonstrated the capability of STM to investigate and probe the properties of nanostructures and nanoscale devices. The imaging of probability distributions represents a leap from a concept of quantum mechanics to a real-space image of a real phenomenon. Techniques developed are constantly being improved as new and more efficient methods are being discovered enabling a greater ability to observe the nature of quantum mechanics on the nano scale.

The limit of STM to operate effectively on flat surfaces has been demonstrated through the investigation of InGaN/GaN multiple quantum well structures. The current methods are not well suited to such a material and so these materials open up the opportunity to develop techniques capable of characterising them. Facet bevelling and etching constitute a material approach to the problem, however, through the development of nanotechnology other methods may be better suited to investigate such materials.

5.1 Further Work

In the high resolution STM and AFM imaging of very flat surfaces ~1nm roughness mechanical vibrations have presented themselves as oscillations in the image. This additional information ultimately reduces the operational resolution of the system. At least three possibilities exist to remove this signal; to isolate the source, to remove the component of the signal after collection, or to compensate for the source mechanically. The passive anti-vibration system employed is comprehensive, however, the signal still persists. It is possible to filter out vibrations using FFT (Fast Fourier Transform) numerical techniques, however, they tend to reduce resolution and introduce artefacts, another method may be to simultaneously collect a separate signal specifically from the vibrational source and subtract it from the signal either before or after measurement.
A third opportunity exists to feedback the vibrational signal into the *Z* control to negate the effect of the vibration or into a piezoelectric support stack to prevent the signal from reaching the SPM tip/probe. This last method would constitute an active anti-vibration system.

SPM probe drift due to the hysteresis and creep in the piezoelectric motors is a significant problem for blind point I/V measurement, it may be possible with modern computer technology to implement an active creep compensation algorithm that continually adjusts the voltage applied to the piezoelectric motors to compensate for creep based upon a set of calibration procedures.

Raster scanning is the conventional method for building an SPM image, it does, however, leave to some undesirable artefacts in the recorded data including directional scarring and creep related drift upon direction change in the raster process. Other continuous motion vector patterns could be used to reduce the effects of abrupt direction changes in the scanning pattern. Possible scanning patterns could be a concentric spiral, variations on Lissajous figures, or Peano or Hilbert space filling curves.

The photoenhanced STM methods used in this research could be further enhanced by scanning through a range of wavelengths of light allowing the transition energies to be

probed and mapped spatially. The techniques could also be improved by improving the resolution of the technique which is limited by modulation frequency and STM scan rates. Greater control of the voltage distribution over the system will reveal the true locations of important data. An ohmic contact on the cleaved edge near to the tunnelling junction would provide this, however, this could make keeping the material clean, difficult, otherwise a suitable ohmic contact as close to the cleaved edge as possible will improve the data accuracy.

The observed signal ratios of the 1st and 2nd wavefunction distributions for the mixed type I – type II quantum well structure are dependant upon illumination intensity. These experiments used a fairly limited range of pump light intensities and observed the reported data with only the maximum $1 Wcm^{-2}$. The emergence of the 2nd wavefunction signal should be observable by varying the pump intensity below that used in these experiments. A suitable conductivity should be achievable before the 2nd wavefunction signal becomes significant.

The InGaN/GaN quantum well materials require a more detailed investigation into the nature of localisation. The preparation of a suitable surface on which to perform STM is key to the use of this technique and with further attention this may be possible. Other techniques are also being used to address this problem and so far have not provided conclusive proof either way. It may be possible to combine the bevelled surface with photoenhanced STM to detect compositional fluctuations. SNOM based near field optical microscopy and photoluminescence may be able to detect compositional fluctuations.